Monthly Notices
of the
ROYAL ASTRONOMICAL SOCIETY

MNRAS **493,** 1044–1062 (2020) doi:10.1093/mnras/stz3390
Advance Access publication 2019 December 4

Nebular spectra of 111 Type Ia supernovae disfavour single-degenerate progenitors

M. A. Tucker [1★†] B. J. Shappee,[1] P. J. Vallely [2] K. Z. Stanek,[2,3] J. L. Prieto,[4,5] J. Botyanszki,[6] C. S. Kochanek,[2,3] J. P. Anderson,[7] J. Brown,[2] L. Galbany,[8] T. W.-S. Holoien [9] E. Y. Hsiao,[10] S. Kumar,[10] H. Kuncarayakti,[11,12] N. Morrell,[13] M. M. Phillips,[13] M. D. Stritzinger[14] and Todd A. Thompson[2,3]

[1]*Institute for Astronomy, University of Hawai'i at Manoa, 2680 Woodlawn Dr., Honolulu, Hi 96822, USA*
[2]*Department of Astronomy, The Ohio State University, 140 West 18th Avenue, Columbus, OH 43210, USA*
[3]*Center for Cosmology and AstroParticle Physics (CCAPP), The Ohio State University, 191 W. Woodruff Avenue, Columbus, OH 43210, USA*
[4]*Núcleo de Astronomía de la Facultad de Ingeniería y Ciencias, Universidad Diego Portales, Av. Ejército 441, Santiago, Chile*
[5]*Millennium Institute of Astrophysics, Santiago, Chile*
[6]*Physics Department, University of California, Berkeley, CA 94720, USA*
[7]*European Southern Observatory, Alonso de Cordova 3107 Casilla 19001, Vitacura, Santiago, Chile*
[8]*PITT PACC, Department of Physics and Astronomy, University of Pittsburgh, Pittsburgh, PA 15260, USA*
[9]*Carnegie Observatories, 813 Santa Barbara Street, Pasadena, CA 91101, USA*
[10]*Department of Physics, Florida State University, 77 Chieftan Way, Tallahassee, FL 32306, USA*
[11]*Finnish Centre for Astronomy with ESO (FINCA), University of Turku, FI-20014 Turku, Finland*
[12]*Tuorla Observatory, Department of Physics and Astronomy, University of Turku, FI-20014 Turku, Finland*
[13]*Las Campanas Observatory, Carnegie Observatories, Casilla 601, La Serena, Chile*
[14]*Department of Physics and Astronomy, Aarhus University, Ny Munkegade 120, DK-8000 Aarhus C, Denmark*

Accepted 2019 October 24. Received 2019 October 21; in original form 2019 March 15

ABSTRACT

We place statistical constraints on Type Ia supernova (SN Ia) progenitors using 227 nebular-phase spectra of 111 SNe Ia. We find no evidence of stripped companion emission in any of the nebular-phase spectra. Upper limits are placed on the amount of mass that could go undetected in each spectrum using recent hydrodynamic simulations. With these null detections, we place an observational 3σ upper limit on the fraction of SNe Ia that are produced through the classical H-rich non-degenerate companion scenario of < 5.5 per cent. Additionally, we set a tentative 3σ upper limit otan He star progenitor scenarios of < 6.4 per cent, although further theoretical modelling is required. These limits refer to our most representative sample including normal, 91bg-like, 91T-like, and 'super-Chandrasekhar' SNe Ia but excluding SNe Iax and SNe Ia-CSM. As part of our analysis, we also derive a Nebular Phase Phillips Relation, which approximates the brightness of an SN Ia from 150 to 500 d after maximum using the peak magnitude and decline rate parameter $\Delta m_{15}(B)$.

Key words: supernovae – general; galaxies – distances and redshifts.

1 INTRODUCTION

Type Ia supernovae (SNe Ia) are utilized across many astronomical disciplines, including the extragalactic distance scale, dark energy studies, and Galactic chemical evolution. Despite their prevalence, the origins of SNe Ia are still unclear even after decades of study. The general consensus is that they are explosions of carbon/oxygen (C/O) white dwarfs (Hoyle & Fowler 1960) with fairly homogeneous properties. For example, the magnitude of SNe Ia at peak is well constrained ($M_{\rm max} \sim -19$, e.g. Folatelli et al. 2010a), and, after correcting for light-curve decline and colour, they have an intrinsic scatter of ∼0.1 mag (e.g. fig. 19, Folatelli et al. 2010a). Many formation mechanisms for SNe Ia have been proposed to reproduce this level of uniformity, which can be grouped into two main categories: the double-degenerate (DD) and single-degenerate (SD) scenarios (see Maoz et al. 2014; Livio & Mazzali 2018; Jha et al. 2019, for reviews on SNe Ia and their progenitors).

The DD scenario consists of two degenerate stars, usually C/O white dwarfs, which induce an SN Ia through accretion, collision, or merger. This can occur due to gravitational wave emission

★ E-mail: tuckerma95@gmail.com
† DOE CSGF Fellow.

(Tutukov & Yungelson 1979; Iben & Tutukov 1984; Webbink 1984), collision/violent merger due to perturbations by external bodies (Thompson 2011; Katz & Dong 2012; Pejcha et al. 2013; Shappee & Thompson 2013; Antognini et al. 2014), accretion from a low-mass white dwarf on to a smaller, higher mass white dwarf (Taam 1980; Livne 1990; Tutukov & Yungelson 1996; Pakmor et al. 2012), or a 'double detonation' where an accreted helium layer detonates and drives the core to detonate (Woosley & Weaver 1994; Fink et al. 2010; Kromer et al. 2010). Due to the intrinsic faintness of both components in these systems, observational confirmation of DD systems is exceptionally difficult (e.g. Rebassa-Mansergas et al. 2018). Some progress has been made on this front, such as bimodal emission in the nebular phase (Dong et al. 2015a; Vallely et al. 2019a) and possible hyper-velocity remnants (Shen et al. 2018; Ruffini & Casey 2019). However, most of the evidence for DD systems comes from the exclusion of SD progenitors (e.g. Shappee et al. 2017).

The SD scenario involves a WD with a nearby non-degenerate companion (Whelan & Iben 1973; Nomoto 1982; Yoon & Langer 2003), usually undergoing Roche lobe overflow (RLOF). The WD accumulates material until reaching critical mass and then explodes. This critical mass is typically considered the Chandrasekhar mass ($M_{\rm ch} \sim 1.4\,{\rm M}_{\odot}$), although sub-$M_{\rm ch}$ explosions, including double detonation scenarios, are also possible (e.g. Livne & Arnett 1995). There are several predicted observational signatures of the SD scenario due to the interaction of the ejecta/explosion and the donor star (Wheeler et al. 1975), including effects on the rising SN Ia light curve (Kasen 2010), soft X-ray emission in the accretion phase (Lanz et al. 2005; Tutukov & Fedorova 2007; Woods et al. 2018), surviving companions with anomalous characteristics (e.g. Canal et al. 2001; Shappee et al. 2013b), and the amount of ^{56}Ni decay products synthesized in the explosion (e.g. Röpke et al. 2012; Shappee et al. 2017).

One of the most promising signatures of an RLOF companion to an exploding WD is emission lines produced by material stripped/ablated from the non-degenerate companion (e.g. Wheeler et al. 1975; Chugai 1986; Marietta et al. 2000; Mattila et al. 2005; Pan et al. 2012), observable in nebular-phase spectra once the SN Ia has faded considerably and becomes optically thin. For example, Boehner et al. (2017) simulated stripping from red giant (RG), main-sequence (MS), and subgiant (SG) stars, finding approximately 0.33, 0.25, and 0.17 $\rm M_{\odot}$, respectively, of stripped mass. Botyánszki et al. (2018) converted these estimates into expected H α luminosities and found that the emitted H α luminosity does not vary linearly with the amount of stripped companion mass, which had been the assumption of previous studies (e.g. Leonard 2007; Shappee et al. 2013a), but instead the relation is closer to logarithmic. Additionally, the H α emission is powered by gamma-ray deposition from the SN Ia ejecta and roughly follows the bolometric luminosity.

In this work, we compile a comprehensive sample of SN Ia nebular spectra spanning 200–500 d after explosion (181–481 d after maximum assuming a rise time of ∼19 d from Firth et al. 2015) to search for the expected emission from stripped/ablated material. We find no such emission in any spectrum in our sample, and place new or updated stripped/ablated mass constraints for each SN Ia. The entirety of similar work in the literature totals 33 SNe Ia (Mattila et al. 2005; Leonard 2007; Lundqvist et al. 2013, 2015; Shappee et al. 2013a; Maguire et al. 2016; Graham et al. 2017; Holmbo et al. 2018; Sand et al. 2018a; Shappee et al. 2018; Tucker et al. 2018; Dimitriadis et al. 2019a; Sand et al. 2019), a fraction of the sample analysed in this work. All SNe Ia included in this study are listed in Table B2 and photometric parameters [$t_{\rm max}$, Δm_{15}, μ, and $E(B-V)_{\rm host}$] are provided in Table B3.

We outline our data sources and reduction techniques, including absolute flux calibration, in Section 2. In Section 3, we discuss our methodology in searching for and placing limits on material stripped from an RLOF companion. Our upper limits on stripped material are provided in Section 4, and our findings are discussed in the context of SNe Ia formation in Section 5. Included in Section 5 are discussions about peculiar SNe Ia and their role in our study including SNe Ia-CSM. Finally, in Section 6, we summarize our results.

2 DATA SOURCES AND REDUCTION

Our sample of 227 spectra of 111 SNe Ia comes from the 40 instruments on the 29 telescopes listed in Table 1. All spectroscopically peculiar SNe Ia are included except for those exhibiting signatures of circumstellar material (SNe Ia-CSM). These SNe Ia exhibit H α emission, but the velocity and magnitude of the emission are inconsistent with material stripped from a nearby companion; instead, these SNe Ia appear to have exploded in a dense circumstellar environment (e.g. SN 2002ic, Wang et al. 2004) and exhibit H α emission before the SN enters the nebular phase (e.g. Silverman et al. 2013). A discussion of SNe Ia-CSM and their role in our results is provided in Section 5.2. For non-CSM SNe Ia, we impose the following criteria when selecting nebular spectra:

(i) Obtained between 200 and 500 d after explosion to maintain consistency with the models of Botyánszki et al. (2018), assuming a typical rise time of $t_{\rm rise} \approx 19$ d (Firth et al. 2015).
(ii) Cover $\pm$1000 km s^{-1} of at least one H or He line in Table 2.
(iii) Have at least one method of absolute flux calibration, outlined in Section 2.3.
(iv) Published, posted, or observed by our team before the submission date of this article (2019 March 15).

The complete list of new and archival spectra is provided in Table B4. Additionally, we include new and archival photometry to supplement our spectral data and analysis. Early-phase photometry ($\lesssim$50 d after maximum light) is used in deriving the photometric properties of each SN Ia using the photometric fitting code `snoopy` (Burns et al. 2011), including time of maximum ($t_{\rm max}$), the decline rate parameter Δm_{15}, extinction along line of sight, and the distance modulus. Late-phase photometry and nebular-phase photometry are used for flux calibrating the nebular spectra and deriving a Nebular Phase Phillips Relation (NPPR). The NPPR approximates the nebular magnitude of an SN Ia given its peak magnitude and decline rate, calibrated to an extensive sample of new and archival SN Ia photometry. A complete description of the NPPR, its derivation, and usage is provided in Appendix A.

2.1 New spectra and photometry

We present 14 new nebular-phase spectra of 13 SNe Ia, of which 10 have no prior published nebular spectra. These spectra were acquired in our ongoing study of SNe Ia progenitors, taken with MagE and IMACS on Baade, MUSE on the VLT, and WFCCD on duPont (see Table 1 for telescope and instrument designations). For the new spectra presented here, each spectrum was reduced

Table 1. All telescopes and instruments utilized in this work. If a reference could not be found for a given instrument, the corresponding instrument website is provided in the table notes.

Telescope	Abbrev.[a]	Instrument	Abbrev.[a]	Ref.	N_{spec}
Australian National University 2.3 m	ANU2.3m	Wide-Field Spectrograph	WiFeS	Dopita et al. (2007, 2010)	7
Calar Alto 2.2 m	CA2.2m	Calar Alto Faint Object Spectrograph	CAFOS	...[b]	1
Calar Alto 3.5 m	CA3.5m	Multi-Object Spectrograph at Calar Alto	MOSCA	...[c]	2
Danish 1.54 m	D1.54m	Danish Faint Object Spectrograph and Camera	DFOSC	Andersen et al. (1995)	1
du Pont Telescope	duPont	Wide Field Reimaging CCD Camera	WFCCD	...[d]	4
		Boller and Chivens Spectrograph	BC	...[e]	1
ESO 1.5 m	ESO1.5m	Boller and Chivens Spectrograph	BC	...[f]	2
ESO 3.6 m	ESO3.6m	ESO Faint Object Spectrograph and Camera	EFOSC1/2	Buzzoni et al. (1984)	11
Harlan J Smith Telescope	HJST	UltraViolet Image Tube Spectrograph	UVITS	Wills et al. (1980)	1
Himalayan Chandra Telescope	HCT	Himalayan Faint Object Spectrograph	HFOSC	...[g]	2
Hubble Space Telescope	*HST*	Faint Object Spectrograph	FOS	...[h]	1
Isaac Newton Telescope	INT	Faint Object Spectrograph (1st Gen.)	FOS1	Breare et al. (1987)	2
Gemini North/South	GN/S	Gemini Multi-Object Spectrograph	GMOS	Hook et al. (2004)	13
Gran Telescopio Canarias	GTC	Optical System for Imaging and low-Intermediate-Resolution Integrated Spectroscopy	OSIRIS	Cepa (2010)	1
Keck I	KeckI	Low Resolution Imaging Spectrograph	LRIS	Oke et al. (1995)	27
Keck II	KeckII	DEep Imaging Multi-Object Spectrograph	DEIMOS	Faber et al. (2003)	9
		Echelette Imager and Spectrograph	ESI	Sheinis et al. (2002)	3
Large Binocular Telescope	LBT	Multi-Object Double Spectrograph	MODS1/2	Pogge et al. (2010)	10
Magellan Baade Telescope	Baade	Inamori-Magellan Areal Camera and Spectrograph	IMACS	Dressler et al. (2011)	3
		Magellan Echellette Spectrograph	MagE	Marshall et al. (2008)	2
Magellan Clay Telescope	Clay	Low Dispersion Survey Spectrograph	LDSS	...[i]	5
Multiple Mirror Telescope	MMT	Blue Channel Spectrograph	BCS	Angel et al. (1979)	6
New Technology Telescope	NTT	ESO Multi-Mode Instrument	EMMI	D'Odorico (1990)	1
		SOFI	...	Moorwood et al. (1998)	1
Palomar 200 inch	P200	Double Spectrograph	DBSP	Oke & Gunn (1982)	4
Shane 3m Telescope	Shane3m	Kast Spectrograph	KAST	Silverman et al. (2013)	11
Southern African Large Telescope	SALT	Robert Stobie Spectrograph	RSS	Buckley et al. (2006)	3
Subaru	Sub	OH-Airglow Suppressor/Cooled Infrared Spectrograph and Camera for OHS	CISCO	Motohara et al. (2002)	3
		Faint Object Spectrograph and Camera	FOCAS	Kashikawa et al. (2002)	2
Tillinghast 1.5 m	Till	FAst Spectrograph for the Tillinghast telescope	FAST	Fabricant et al. (1998)	7
Telescopio Nazionale Galileo	TNG	Device Optimized for LOw RESolution	DOLORES	Molinari et al. (1999)	2
Very Large Telescope	VLT	FOcal Reducer and low dispersion Spectrograph	FORS1/2	Appenzeller et al. (1998)	43
		Multi-Unit Spectroscopic Explorer	MUSE	Bacon et al. (2010)	8
		XSHOOTER	XSH	Vernet et al. (2011)	16
William Herschel Telescope	WHT	Intermediate dispersion Spectrograph and Imaging System	ISIS	Jorden (1990)	5
		ACAM	...	Benn et al. (2008)	1
		Faint Object Spectrograph (2nd Gen.)	FOS2	Breare et al. (1987)	6
Total	29		40		227

[a] Abbreviations used in Table B4.
[b] http://w3.caha.es/CAHA/Instruments/CAFOS/cafos_overview.html
[c] http://www.caha.es/CAHA/Instruments/MOSCA/index.html
[d] http://www.lco.cl/telescopes-information/lco/telescopes-information/irenee-du-pont/instruments/website/wfccd/wfccd-manuals
[e] http://www.lco.cl/telescopes-information/irenee-du-pont/instruments/website/boller-chivens-spectrograph-manuals/user-manual/the-boller-and-chivens-spectrograph
[f] http://www.ls.eso.org/lasilla/Telescopes/2p2/E1p5M/BC/BC.html
[g] https://www.iiap.res.in/iao/hfosc.html
[h] http://stecf-poa.stsci.edu/poa/FOS/fos_doc_access.html
[i] http://www.lco.cl/telescopes-information/magellan/instruments/ldss-3

Table 2. Line luminosities for both the hydrogen-rich (H-rich) model and the helium-rich (He-rich) model corresponding to the MS38 and helium models from Botyánszki et al. (2018). Helium lines are given letter designations to ease identification in Table B5. FWHM refers to the expected FWHM of a line profile broadened by $\sim 10^3$ km s^{-1}.

Line	λ	L_{200} (10^{38} erg s^{-1})	FWHM (Å)
H-rich model			
H γ	4341 Å	0.271	14.5
H β	4831 Å	4.38	16.1
He I-a	5875 Å	4.27	19.6
H α	6563 Å	68.0	21.9
He I-b	6678 Å	2.24	22.3
He I-c	1.08 μm	10.5	36.0
Paβ	1.281 μm	14.6	42.7
Paα	1.875 μm	14.6	62.5
He I-d	2.06 μm	8.48	68.7
He-rich model			
He I-a	5875 Å	8.26	19.6
He I-b	6678 Å	6.90	22.3
He I-c	1.08 μm	18.2	36.0
He I-d	2.06 μm	12.9	68.7

using telescope and instrument-specific pipelines, if available, otherwise typical IRAF[1] tasks were used. The spectra acquired with MagE/Baade were reduced with a pipeline provided by the Carnegie Observatories[2] (Kelson et al. 2000; Kelson 2003), with the exception of standard star calibrations and stitching together each echellette spectrum, which was done with custom PYTHON routines. For newly presented MUSE data acquired as part of the AMUSING survey (Galbany et al. 2016), spectra were extracted in a 1" circular aperture at the SN Ia location using the PyMUSE package (Pessa et al. 2018), and corrected for host galaxy contributions using a background annulus extending from 2" to 3". New IMACS/Baade spectra were reduced with typical IRAF procedures including bias subtraction, flat-field correction, arc lamp exposures for wavelength calibration, and standard star observations to correct for instrument and atmospheric response.

For absolute flux calibrations, we also include nebular photometry for any SNe Ia in our sample. This includes new observations and reprocessed archival images for which we could not find a published magnitude. New photometry includes *V*-band images taken with FORS2, *r*-band images from MODS1, and *BVRI* images from WFCCD. Archival imaging includes *UBVRI* imaging from FORS1/2 and *BVRgri* imaging from EFOSC2 (Table B6). All images are bias subtracted and flat-field corrected before performing aperture photometry with the `IRAF` *apphot* task. For targets with $\delta \geq -30^\circ$, photometry from the Pan-STARRS Stack Object catalogue[3] (Chambers et al. 2016; Flewelling et al. 2016) was used in calibrating the images, otherwise *Gaia* DR2 photometry (Gaia Collaboration 2016, 2018; Riello et al. 2018) was used. When transforming reported magnitudes to other photometric systems, Tonry et al. (2012) and Evans et al. (2018) were used for Pan-STARRS and *Gaia*, respectively. The only exceptions to this procedure are the *B*-band FORS2/VLT images, which are calibrated using the reported photometric zero-points.[4]

2.2 Archival spectra and photometry

The primary sources of our archival spectra and photometry are the Berkeley SuperNova Ia Program[5] (Silverman et al. 2012, 2013), the Center for Astrophysics Supernova Data Archive[6] (Riess et al. 1999; Jha et al. 2006; Matheson et al. 2008; Blondin et al. 2012), the Carnegie Supernova Project[7] (CSP; Hamuy et al. 2006; Contreras et al. 2010; Folatelli et al. 2010a; Stritzinger et al. 2011; Folatelli et al. 2013; Krisciunas et al. 2017; Phillips et al. 2019), the 100IAs project (Dong et al. 2018a), the ANU WiFeS SuperNovA Program (Childress et al. 2016), and the All-Sky Automated Survey for SuperNovae (ASAS-SN; Shappee et al. 2014a; Holoien et al. 2017a, b, c, 2019, Vallely et al., Chen et al., in preparation). The majority of the publicly available data were retrieved using the Open Supernova Catalog (OSC; Guillochon et al. 2017) and the Weizmann Interactive Supernova data REPository (WISeREP; Yaron & Gal-Yam 2012). All data provided by these sources are already reduced with the exception of precise spectral flux calibration, which we outline in Section 2.3. Additionally, we supplement these sources with archival data obtained from telescope data bases, including the Keck Observatory Archive[8] (KOA), the ESO Science Archive Facility [9] (ESO SAF), the Isaac Newton Group Archive,[10] and the Gemini Observatory Archive[11] (GOA). Information on all the spectra in this study is presented in Table B4.

Data reduction and calibration were performed as uniformly as possible across all sources of spectra. Data retrieved from public archives were already reduced, with the exception of absolute flux calibration. The reduction of data retrieved from telescope archives was generally less complete. All spectra retrieved from the ESO SAF were already reduced (excluding flux corrections) with the exception of FORS1/2 data. For any ESO SAF data reduction, both spectroscopy and photometry, we used the ESO SAF `esorex` data reduction pipeline (Freudling et al. 2013).

Spectra obtained from the KOA and GOA were not reduced prior to retrieval and had to be manually reduced. Recent LRIS spectra were reduced using Lpipe,[12] while the older LRIS and DEIMOS data were reduced using the LowRedux/XIDL pipeline.[13] Gemini North/South GMOS spectra were reduced with the GMOS Data Reduction Cookbook.[14]

We manually reduced any unreduced spectra for which no pipeline exists using standard IRAF procedures. Images were flat-fielded and bias subtracted using archival calibration images taken near the epoch of observation, and wavelength calibrated with arc lamp exposures. Spectrophotometric standard star observations were used to correct for telescope/instrumental artefacts,

[1] http://iraf.noao.edu/
[2] http://code.obs.carnegiescience.edu/mage-pipeline
[3] http://archive.stsci.edu/panstarrs/stackobject/search.php
[4] https://www.eso.org/observing/dfo/quality/FORS2/qc/zeropoints/zeropoints.html
[5] http://heracles.astro.berkeley.edu/sndb/
[6] https://www.cfa.harvard.edu/supernova/SNarchive.html
[7] http://csp.obs.carnegiescience.edu/
[8] https://koa.ipac.caltech.edu/
[9] http://archive.eso.org/cms.html
[10] http://casu.ast.cam.ac.uk/casuadc/ingarch/query
[11] https://archive.gemini.edu/
[12] http://www.astro.caltech.edu/ dperley/programs/lpipe.html
[13] http://www.ucolick.org/ xavier/LowRedux/
[14] http://ast.noao.edu/sites/default/files/GMOS_Cookbook/

atmospheric effects, and to place each spectrum on a reliable relative flux scale.

2.3 Accurate flux calibration

For our analysis in Section 3, the spectra must be on a reliable absolute flux scale. While calibrating spectra with spectrophotometric standard stars places these spectra on a dependable relative flux scale, slit losses, atmospheric conditions, and other effects can cause the resulting spectra to deviate from an absolute flux scale. To scale a spectrum to the absolute scale, we employed equation (7) from Fukugita et al. (1996) to calculate synthetic photometry from the spectra. The spectra are then scaled so that the synthetic photometry matches the observed photometry. There were several different sources of photometry used to calibrate the spectra. In order of preference and reliability, with accuracy estimates in given parentheses:

(i) For spectra with acquisition images taken at the time of observation, we scale the entire spectrum to match these photometric observations, usually in the *V* or *r* filters (∼5–10 per cent).

(ii) If acquisition images are unavailable, we next tried to use photometry within ±5 d of the spectral observations. Photometry in all available filters within this temporal limit was used in the flux calibration (∼10–15 per cent).

(iii) If no photometric data were available within ±5 d, we searched for photometry within ±50 d. If at least three photometric data points fell within this time span, we linearly interpolated to estimate the magnitude at the time of the spectral observation (∼15–20 per cent).

(iv) If none of these were available, the nebular *BVR* magnitude was estimated with the NPPR and used to calibrate the spectrum (see Appendix A, ∼20 per cent).

We required > 90 per cent of the filter's transmission curve be covered by the observed spectrum for viable calibrations. If only a single filter was available, the entire spectrum was scaled to match the observation. If two filters were available for flux calibration, a simple linear fit was applied to the scale factors. If >3 filters were available, we use spline fits with fixed endpoints to ensure a robust flux correction across the entire spectrum. After placing the spectrum on an absolute flux scale, we correct for host galaxy and Milky Way reddening using the $E(B-V)_{\rm host}$ derived from the light-curve fits. We implement a Fitzpatrick (1999) extinction law and a Schlegel et al. (1998) Milky Way dust map for our reddening corrections. We assume $R_{\rm V} = 3.1$ unless stated otherwise (see Appendix B).

2.4 Sample demographics

After collecting all nebular spectra that meet our temporal and calibration requirements, our sample consists of 111 SNe Ia (Table B2). Due to the comprehensive nature of our search for nebular spectra, our sample is inherently biased towards brighter or peculiar SNe Ia as these objects have a higher likelihood of being observed in the nebular phase. This effect is readily apparent in Fig. 1, where the Δm_{15} values of SNe Ia in our sample are compared to a purely photometric sample from the Lick Observatory Supernova Search (LOSS; Li et al. 2000; Ganeshalingam et al. 2010). Similar to the luminosity bias, we are biased to lower redshift SNe Ia with a median redshift of $z_{\rm med} \approx 0.015$. We provide the temporal distribution for our set of nebular spectra in Fig. 2, including distributions for the earliest and latest spectra for each SN Ia. As expected, the number of spectra generally declines at later phases due to the supernovae fading from view.

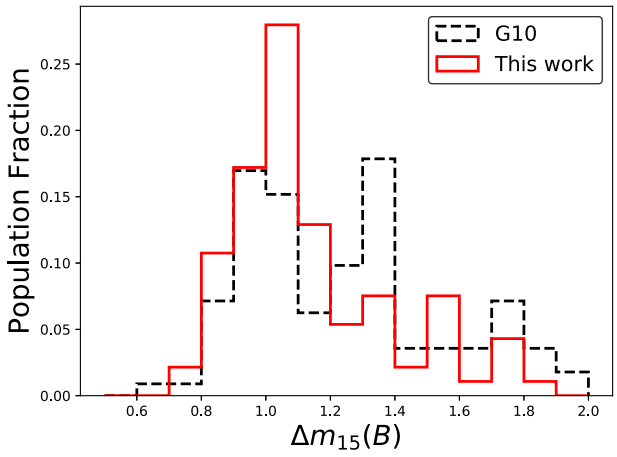

Figure 1. Distribution of $\Delta m_{15}(B)$ in our sample compared to the photometric sample from LOSS (Ganeshalingam et al. 2010). As expected, the nebular sample is biased towards brighter and broader SNe Ia.

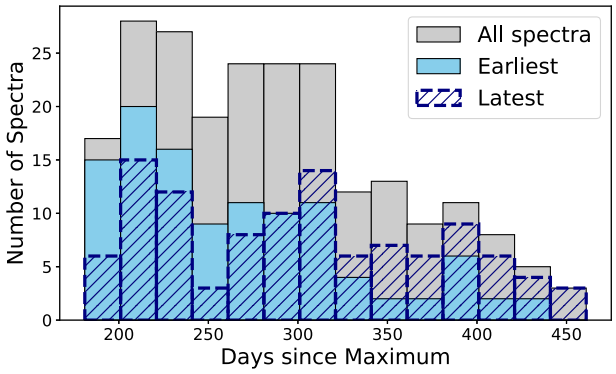

Figure 2. The number of spectra per day since maximum for three distributions: (1) all spectra in our sample (grey), (2) the earliest spectrum for each SN Ia (light blue), and (3) the latest spectrum for each SN Ia (dark blue, hatched).

3 SEARCHING FOR EMISSION FROM STRIPPED COMPANION MATERIAL

Prior to the work of Botyánszki et al. (2018), the majority of unbound mass limits in the literature utilized the work of Mattila et al. (2005) and Leonard (2007) to compute stripped mass limits from comparing observed spectra to expected Hα luminosities. Several subsequent studies have adopted these methodologies in their work (e.g. Maguire et al. 2016; Graham et al. 2017) with notable success in ruling out hydrogen-rich companions. Yet the models of Mattila et al. (2005) had several shortcomings in observational implementation. In particular, Leonard (2007) assumed a linear scaling between the amount of unbound companion mass and the corresponding Hα luminosity.

Botyánszki et al. (2018), using the MS38 model (an MS star undergoing RLOF) from Boehner et al. (2017), instead found that the emitted Hα luminosity scales logarithmically with the amount of stripped mass. Additionally, Botyánszki et al. (2018) computed a simplified helium-star model, where all the stripped mass from the MS38 model is replaced with helium instead of

Solar abundance material. This is not a true helium-star model, as helium-star companions are expected to have lower amounts of stripped mass than their hydrogen-rich counterparts and a modestly different velocity distribution (e.g. Pan et al. 2012), but it provides a starting point for calculating limits on the amount of unbound helium in an SN Ia spectrum.

While the models of Botyánszki et al. (2018) clarify the mass–luminosity scaling issue and expand to helium emission, they share two other shortcomings with the models of Mattila et al. (2005): the requirement of using H α to constrain the amount of unbound mass, and only calculating the expected H α luminosity at a single epoch (200 d post-explosion for Botyánszki et al. 2018 and 350 d post-maximum for Mattila et al. 2005). In the following sections, we discuss our stripped mass limits given these limitations.

3.1 Expanding on these models

For SNe Ia with star-forming host galaxies, the region around H α can be contaminated by narrow host galaxy H α and N II emission lines, which complicates setting limits on H α emission. However, the unbound material has emission lines besides H α, including H β, H γ, and the Paschen series. Assuming roughly Solar metallicity, the stripped material will also exhibit prominent He I lines in the optical and NIR (Botyánszki et al. 2018). We provide the luminosities for each of these lines in Table 2 at $(t - t_0) = 200$ d from explosion for the hydrogen-rich (H-rich) model using the same MS38 model as Botyánszki et al. (2018). Additionally, we supply similar data for the simplified helium-star model from Botyánszki et al. (2018), which we refer to as the He-rich model.

Botyánszki et al. (2018) estimated the line luminosity at 200 d as a function of the amount of stripped mass ($M_{\rm st}$). Table 2 provides the expected luminosity $L_{200}(M_{\rm st})$ of various lines for $M_{\rm st} = 0.25\,{\rm M}_\odot$. The dependence on the amount of stripped mass is well approximated by $\log_{10} L_{200}(M) \simeq \log_{10} L_{200}(0.25\,{\rm M}_\odot) + 0.17M - 0.2M^2$, where $M = \log_{10}(M_{\rm st}/{\rm M}_\odot)$. Botyánszki et al. (2018) do not provide the time dependence of the line emission specifically, but note that the H α emission is proportional to the Fe III emission over the $200 < (t - t_0) < 500$ d period they consider. Utilizing the synthetic spectra models from Botyánszki & Kasen (2017), we find that the Fe III emission is well fitted by an exponential (Fig. 3), which leads to an estimate for the line luminosity of

$$\log_{10} L(M,t) = \log_{10} L_{200} + 0.17M - 0.20M^2 - \left(\frac{t - t_0}{200\ {\rm d}} - 1\right) \quad (1)$$

provided $M_{\rm st} < 2\,{\rm M}_\odot$. This should hold well for the Balmer lines, and is at least a better approximation for the Paschen and He I lines than assuming that their luminosities are temporally constant.

The models from Botyánszki & Kasen (2017) used to derive the luminosity decay in Fig. 3 are truncated at 400 d after explosion. However, the ratio between Fe III and H α remains roughly constant out to 500 d after explosion (Botyánszki et al. 2018). To incorporate spectra taken between 400 and 500 d after explosion, we extrapolate the exponential fit to the later epoch. Since the models used to derive the Fe III emission decay are generalized to non-peculiar SNe Ia and independent of any possible H or He emission, we consider this assumption valid. However, we do not extrapolate to earlier epochs for two reasons. The onset of the nebular phase is not clearly defined in the literature (e.g. Black et al. 2016), leading to ambiguities in when stripped material might become visible. Additionally, the luminosities for stripped material given in Table 2 are taken from

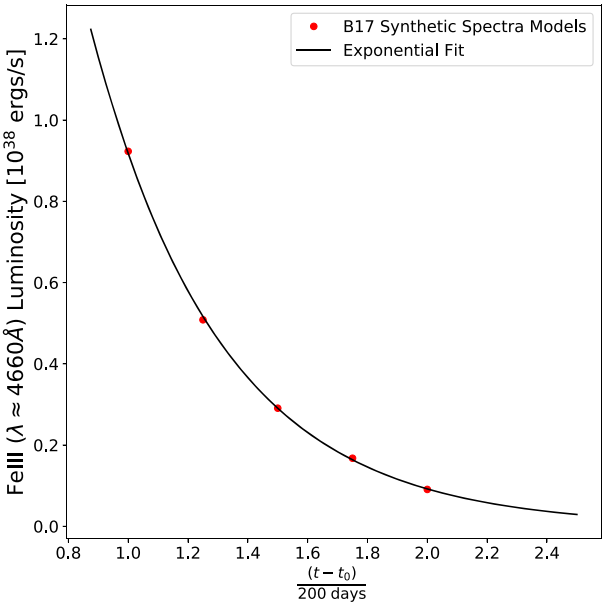

Figure 3. Peak luminosity of the Fe III line (red points) versus days since explosion ($t - t_0$) from the time-dependent SN Ia spectral models of Botyánszki & Kasen (2017) and the exponential fit (black line).

Botyánszki et al. (2018), who explicitly state that their models are valid in the regime of $200 \leq (t - t_0) \leq 500$ d. If these concerns are mitigated by future work, our results can be expanded to include objects with earlier spectra.

3.2 Placing statistical limits on stripped mass

Once each spectrum is flux calibrated and corrected for the reddening, we place statistical limits on the presence of emission lines listed in Table 2, roughly following the methods of Leonard (2007). Each spectrum is rebinned to the approximate spectral resolution, and the spectral continuum is fitted with a second-order Savitsky–Golay polynomial (Press et al. 1992), excluding pixels within $2 \times$ FWHM of line centres to prevent biasing our continuum fit, as done in previous studies (e.g. Maguire et al. 2016). However, since we are inspecting multiple lines for emission signatures, we apply our continuum model in velocity space instead of wavelength space to incorporate this modification.

No single continuum width adequately fits the continuum for all SNe Ia in our sample, especially considering the spectroscopic and temporal diversity. We tailored the continuum fit width for each spectrum based on the observed SN Ia expansion velocity, measured from the prominent emission lines in the spectrum. Since most of the major emission lines in nebular SNe Ia are blended to some extent (e.g. Mazzali et al. 2015, fig. 5), we compute the weighted average from the fitted line profiles assuming a Gaussian emission profile + linear continuum. The lines considered for deriving the expansion velocity are the major Fe II, Fe III, and Co III lines indicated by the vertical dashed lines in Fig. 4. If the SNR of the spectrum is too low for the widths of at least two lines to be measured confidently, we assume a typical width of 3000 km s^{-1}. For velocities lower than this value, we risk biasing our continuum fit to include possible weak emission, and implement 3000 km s^{-1} as a strict lower bound. Additionally, since SNe Iax are known to have narrow line profiles in the nebular phase compared to typical SNe Ia (Foley et al. 2016), we adopt this lower bound for SNe Iax

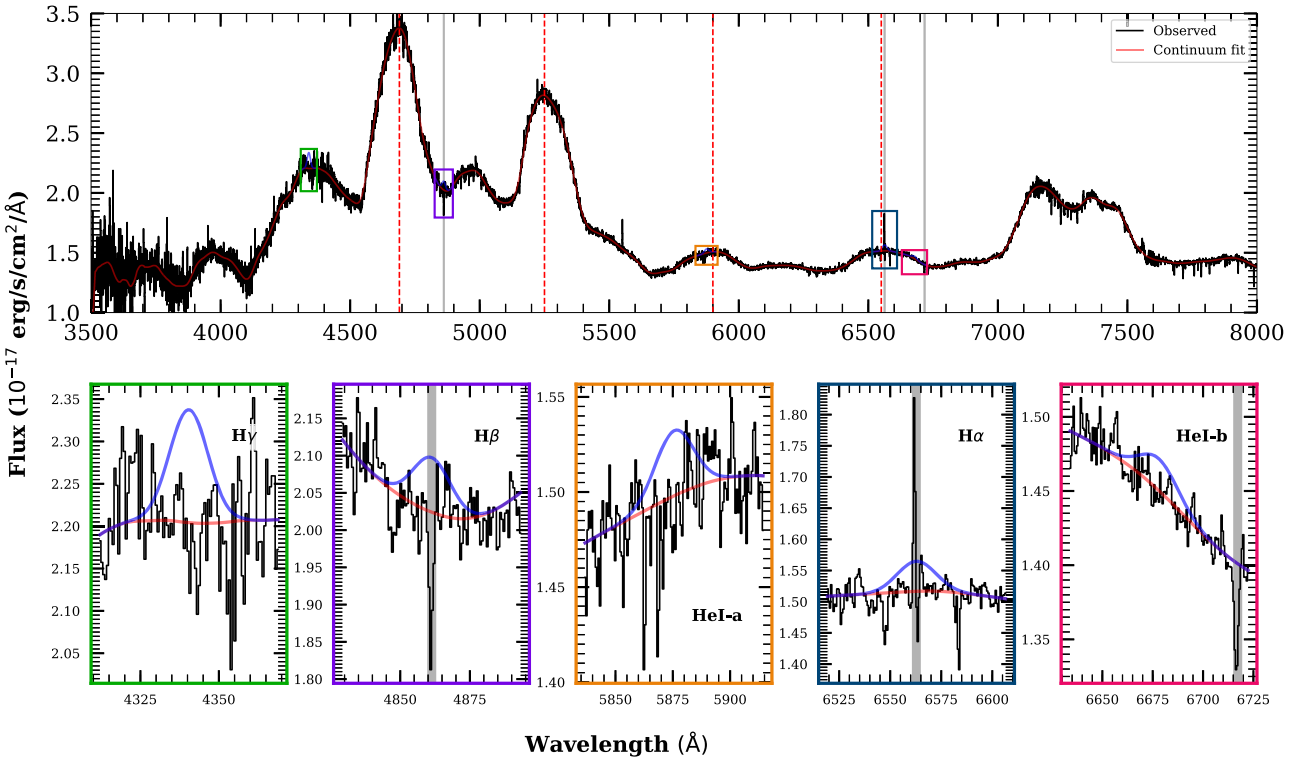

Figure 4. Nebular-phase spectrum (black), continuum fit (red), and derived 10σ flux limits (blue) for the Baade/MagE + 295 d spectrum of SN 2015F. The bottom panels show the regions near each possible emission line from Table 2 and correspond to the coloured boxes in the top panel. The grey shaded areas indicate masked spectral regions due to host galaxy contamination or instrumental effects, and the vertical dashed lines indicate SNe Ia emission lines used to estimate the smoothing width for each spectrum (see Section 3). Similar spectral cut-outs for all SNe Ia are included as supplementary figures (see Appendix B).

as well. Because these velocities are simply a proxy for the width of the continuum fit, this method neglects the intricacies of SNe Ia emission profiles, especially since spectroscopically bimodal SNe Ia are not uncommon (Dong et al. 2015a; Vallely et al. 2019a). However, these complications are unimportant for our analysis, and we consider these simple velocity approximations adequate.

When applying the continuum fit to each spectrum, we minimize biasing our continuum by using 3σ clipping to exclude narrow host galaxy lines, telluric absorption, or instrumental artefacts. After fitting the continuum model to the data, we subtract off this continuum and inspect the residuals for emission-line signatures from unbound companion material. For each line in Table 2, we compute 10σ bounds on the integrated line flux in each region similar to equation (4) from Leonard & Filippenko (2001). However, for flux-calibrated spectra,

$$F(10\sigma) \equiv EW(10\sigma) \times C_\lambda = 10 C_\lambda \Delta I \sqrt{W_{\rm line} \Delta X}, \quad (2)$$

where $F(10\sigma)$ is the 10σ upper limit on the integrated flux, $EW(10\sigma)$ is the corresponding upper limit on the equivalent width, C_λ is the continuum flux at wavelength λ, ΔI is the RMS scatter around a normalized continuum, $W_{\rm line}$ is the width of the line profile, and ΔX is the bin size of the spectrum. We assume that $W_{\rm line}$ is equal to the FWHM of an $\sim$1000 km s^{-1} emission line and provide these values in Table 2. Equation (2) can be rewritten as

$$F(10\sigma) = 10\, \Delta f_\lambda\, \mathcal{F}^{-1} \sqrt{W_{\rm line} \Delta X}, \quad (3)$$

where Δf_λ is the 1σ RMS scatter of the spectrum around the continuum in flux units (erg s^{-1} cm^{-2} Å^{-1}) and $\mathcal{F}^{-1}$ is the correction term for masked pixels (see Section 3.3). Our 10σ statistical limit may seem overly conservative but it does correspond to a line profile that would be visibly obvious (e.g. Fig. 5). Additionally, other studies have run injection-recovery tests to determine the true detection threshold for $\sim$1000 km s^{-1} emission lines in SNe Ia nebula spectra and a purely statistical $F(3\sigma)$ is difficult to recover (e.g. Sand et al. 2018a).

$F(10\sigma)$ is then converted into a luminosity via the distance moduli listed in Table B3. Distance moduli computed from the SN Ia light curves are used except where more reliable methods are available, such as Cepheid or Tip of the Red Giant Branch distances. Equation (1) is inverted to numerically calculate a limit on $M_{\rm st}$, which we consider as a conservative upper bound on the amount of mass removed from a non-degenerate companion undergoing RLOF. This is done for each H/He line, retaining the best mass limit for both the H-rich and He-rich models. Note that the strictest mass limit for each model can come from different spectra, as each spectrum will have varying amounts of contamination from host galaxy and telluric lines.

3.3 Mitigating host galaxy emission and other contaminants

Due to the comprehensive nature of our sample, some spectra have poor-quality, significant host-galaxy emission and/or other contaminants. Pixels affected by host-galaxy emission, telluric absorption, or instrumental artefacts are masked in the ensuing flux limit calculation, ensuring only informative pixels are used in placing our flux upper limit. Masking these pixels also reduces the effective number of pixels used in the non-detection limit calculation and weakens our statistical limit. In equation (3), we include the masked pixel correction term $\mathcal{F}^{-1}$ from Tucker et al. (2018) to correct our limit to a more robust estimate. Concisely,

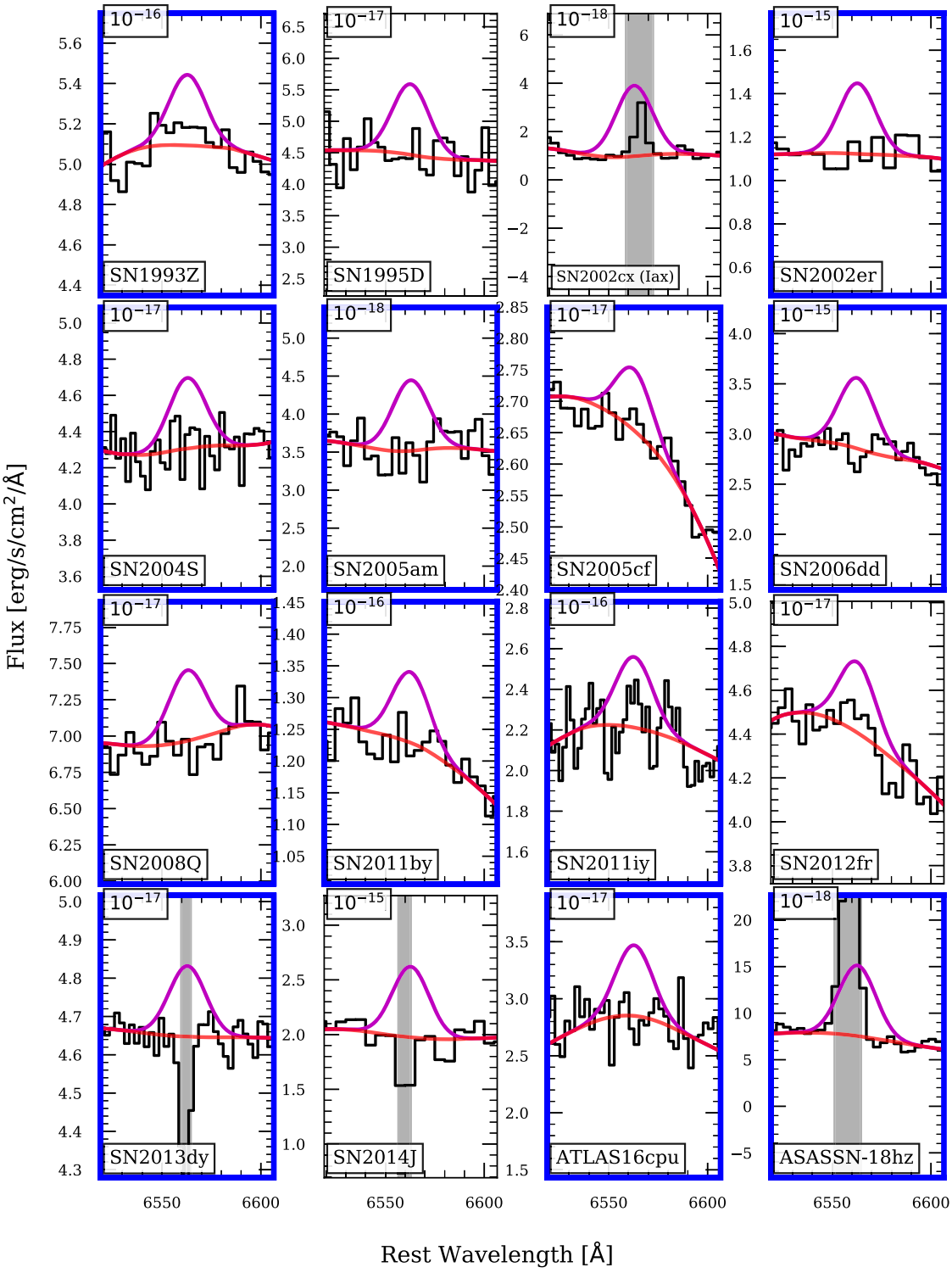

Figure 5. Randomly selected cut-outs around H α for a portion of the SNe Ia in this work, including the observed spectrum (black), the continuum fit (red), and the empirical 10σ line limit (purple). The scale for each spectrum is denoted in the top left of each panel. The light grey areas mark masked regions (see the text) and the completely grey boxes signify SNe Ia with no spectra covering the wavelength range. The thick blue axes indicate that this spectrum was used for the best M_{st} limit provided in Table B5. Cut-outs for all SNe Ia and all H/He lines are provided as supplementary material (see Appendix B).

the correction term $\mathcal{F}$ is the fraction of unmasked line flux to total line flux ($\mathcal{F} \in [0, 1]$). Thus, masked pixels decrease $\mathcal{F}$ and increase $F(10\sigma)$, but the effect is weighted by the location of the masked pixels relative to the line centre. For example, the masked narrow host galaxy H α and H β in the bottom panels of Fig. 4 have larger effects on $\mathcal{F}$ than the masked [S II] line at 6713 Å since [S II] is on the outskirts of the He I-a line profile. Masking is only implemented when the derived $F(10\sigma)$ is not representative of the true flux limit

due to contaminated pixels; we leave weak or minor contamination unmasked as it only solidifies our conservative flux limit and does not introduce extra steps in our analysis.

Another difficulty occurs when the expected emission line is blended with the edge of a steep SN spectral feature. This is especially problematic for 91bg-like and Iax SNe that have intrinsically narrow emission-line profiles. If the continuum near H/He varies by more than the amplitude of our flux limit over its FWHM, we increase our flux limit to match the continuum level variation. This results in an unambiguous line profile that would be definitively detected and prevents questionable limits from being included in our statistical analysis.

Some spectra in our study have resolutions of the order of $\sim$500 km s^{-1}, which approaches the lower end of the expected stripped mass velocity distribution (e.g. Boehner et al. 2017). If broad, unresolved H emission was present in a spectrum, we confirm the host galaxy source with other typical galaxy emission lines such as [O II] (3727 Å), [O III] (4959, 5007 Å), [N II] (6548, 6583 Å), and [S II] (6713, 6731 Å). Any unresolved Hα emission with velocity widths $\gtrsim$300 km s^{-1} had at least one other unresolved galaxy emission line in the spectrum, indicating the observed H emission was not from stripped material. Additionally, the recent discovery of broad Hα emission in ATLAS18qtd (Prieto et al. 2019) affirms our treatment of galaxy emission lines, as none of the galaxy emission lines discussed previously were present in the discovery spectrum (see Section 5).

4 RESULTS

We find no evidence of emission from stripped/ablated companion material in any of our nebular-phase spectra. Fig. 4 provides an example Baade/MagE spectrum of SN 2015F at +295 d after maximum light, including the observed spectrum, the continuum fit, and the 10σ flux limits for each line. We provide a random selection of Hα flux limit cut-outs in Fig. 5, and the spectral cut-outs for all the H and He lines are provided as supplementary material.

The distribution of stripped mass limits is shown for the H-rich and He-rich cases in Figs 6 and 7, respectively, with colour-shaded regions indicating the expected amounts of stripped mass from various studies in the literature. Fig. 8 shows the H-rich results using the methods and models of Mattila et al. (2005) and Leonard (2007) for a comparison with previous estimates. Table B5 gives the phases, flux limits, and derived H-rich and He-rich mass limits for each SN Ia in our study.

We include the range of mass estimates from an H-rich RLOF companion in Figs 6 and 8 as shaded regions for main-sequence (MS, blue), subgiant (SG, green), and red giant (RG, red) companions taken from Marietta et al. (2000), Pan et al. (2012), and Boehner et al. (2017). We take 0.15 M$_\odot$ as the minimum amount of mass stripped from a companion in the SD scenario, SNe Ia with $M_{\rm st,H} < 0.15\,{\rm M}_\odot$ are considered unlikely to have an H-rich SD progenitor system.

For the He-rich SD channel, only Pan et al. (2012) and Liu et al. (2013a) have published models. We include their expected values for mass stripped from an RLOF helium-star companion in Fig. 7 as the magenta-shaded area (Liu et al. 2012) and the cyan line (Pan et al. 2012). However, there are several caveats when considering the He-rich model. The expected line luminosities given in Table 2 are for 0.25 M$_\odot$ of stripped He-rich material, more mass than expected for a true He-donor star. We compare our mass limits to the dedicated He-rich models from Pan et al. (2012) and Liu et al. (2013a) and take a limit of $M_{\rm st,He} < 0.023\,{\rm M}_\odot$ as our upper limit for He-rich SD systems.

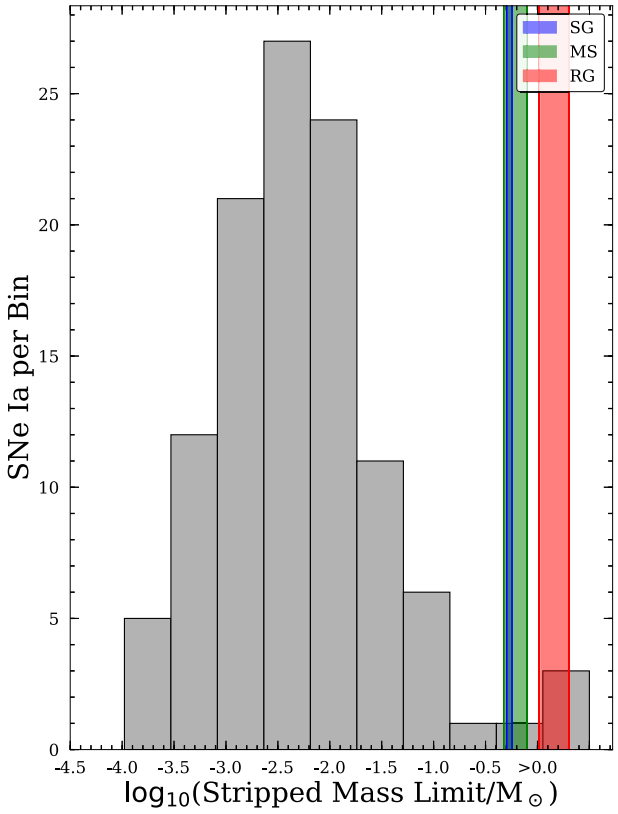

Figure 6. Distribution of mass limits on stripped H-rich material for all SNe Ia in our sample. The colour-shaded areas indicate expected amounts of unbound mass for subgiant (SG, blue), main-sequence (MS, green), and red-giant (RG, red) companions, taken from Marietta et al. (2000), Pan et al. (2012), and Boehner et al. (2017).

If we assume that SNe Ia with $M_{\rm st,H} < 0.15\,{\rm M}_\odot$ and $M_{\rm st,He} < 0.023\,{\rm M}_\odot$ exclude H-rich and He-rich SD progenitor systems, respectively, we can constrain the observed fraction of SD systems. Based on the non-detections in our sample, we can place observed upper limits on the fraction of SD SNe Ia. For a binomial distribution with N trials and no successes, the upper limit f at a confidence level P can be expressed as

$$f < 1 - (1 - P)^{(N+1)^{-1}} \quad (4)$$

with the results for our sample provided in Table 3. $f_{1\sigma}$ and $f_{3\sigma}$ correspond to the 1σ and 3σ fractional upper limits on SD SNe Ia, respectively. For our null detections of unbound mass emission, we place statistical constraints on the fraction of SNe Ia that can form through the classical SD scenario for H-rich and He-rich companions. We do not consider SNe Ia with inadequate limits on $M_{\rm st}$ 'successes', as the spectra do not show any evidence of the expected emission signatures, so these objects are simply omitted from our statistical analysis.

5 DISCUSSION

5.1 Statistical implications

With our updated modelling and comprehensive sample, we place strict constraints on the fraction of SNe Ia that can form through

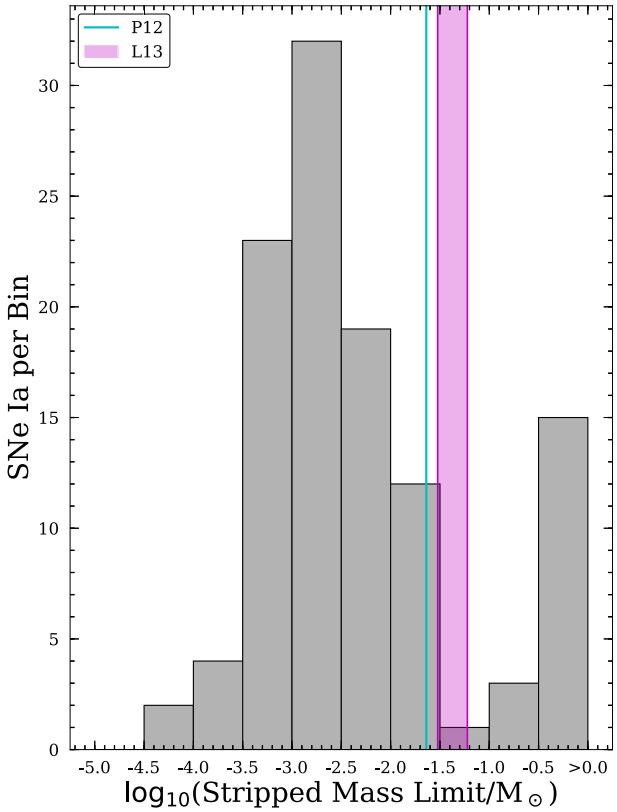

Figure 7. Similar to Fig. 6, except for the He-rich model. The magenta-shaded region corresponds to stripped mass estimates from Liu et al. (2013a) and the cyan line marks the estimate from Pan et al. (2012).

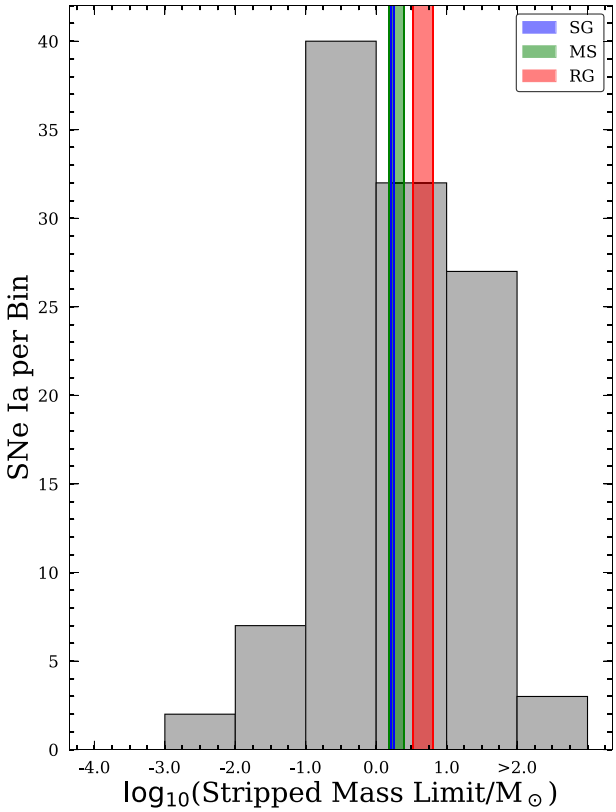

Figure 8. Similar to Fig. 6, except using the models of Mattila et al. (2005). The assumed linear scaling between luminosity and stripped mass leads to higher derived M_{st}.

the classical SD scenario. At most, ∼6 per cent of SNe Ia (at 3σ confidence) can stem from the H-rich formation channel, placing the majority of the production of SNe Ia on the DD channel, unless a modification on the SD scenario can prevent nearly all SNe Ia from exhibiting these expected H and He emission signatures such as the spin-up/spin-down scenario (Di Stefano et al. 2011; Justham 2011; Meng & Podsiadlowski 2013). Considering the simplest case of only spectroscopically normal SNe Ia, we place a 1σ (3σ) upper limit on SD progenitors of < 1.3 per cent (< 6.6 per cent). The full statistical results are provided in Table 3, and we use the *Normal+91T+91bg + SC* sample as the most representative sample from our survey. Unfortunately, our sample prevents an analysis of underluminous versus overluminous SNe Ia, as we are biased towards brighter SNe Ia (Fig. 1). This highlights the importance of volume-limited surveys such as 100IAs (Dong et al. 2015a). Still, these stringent constraints on the observed rate of SD SNe Ia provide strong evidence for the DD channel producing the majority of SNe Ia.

We separately consider spectroscopic subclasses at the extreme edges of the Phillips Relation. Because these SNe Ia are thought to be on the edges of typical SN Ia formation, we compare the derived stripped mass limits to the same expected stripped mass values as normal SNe Ia. Our sample has eight 91bg-like and five 91T-like SNe Ia, for which we place 1σ (3σ) upper limits on H-rich SD progenitors at < 12.0 per cent (< 48.2 per cent) and $<$ 17.4 per cent (< 62.7 per cent), respectively. It is worth mentioning that the stripped mass models assume a normal SN Ia explosion and the effects of underluminous and overluminous SNe Ia on the amount of stripped material are yet to be investigated.

For SNe Iax and 'super-Chandrasekhar' (SC) SNe Ia, it is worth discussing their characteristics and applicability to our study. The Iax subtype (Foley et al. 2013) is thought to stem from an entirely different formation mechanism and is not observed to enter a nebular phase but instead has photospheric properties (Foley et al. 2016). Our study includes four such systems: SNe 2002cx, 2005hk, 2008A, and 2012Z. Liu et al. (2013b) investigated the expected values of unbound mass for these systems if in an SD system, finding significantly lower values of $M_{st,H} \approx 0.013$–$0.016\,M_\odot$ compared to the typical $\sim$0.1–0.5 $M_\odot$ range. All Iax SNe Ia in our sample have $M_{st,H} < 0.013\,M_\odot$, so the statistics are unchanged if the more stringent mass limit is employed. However, even if material is unbound from non-degenerate donor stars in these SNe Ia, it is unclear if this material would be visible at late times. For these reasons, our main statistical analysis excludes these objects.

Our sample also includes four 'super-Chandrasekhar' (SC) SN Ia explosions (SNe 2006gz, 2007if, 2009dc, and SNF 20080723-012), where the inferred ejecta mass, M_{ej}, is higher than the Chandrasekhar mass of $\approx 1.4\,M_\odot$ (e.g. Howell et al. 2006; Scalzo et al. 2019), although the nomenclature is currently debated (Chen et al. 2019). The preferred formation theory of SC SNe Ia involves a DD merger of two WDs with a combined mass above the Chandrasekhar mass (Tutukov & Yungelson 1994; Howell 2001), although SD progenitors have also been proposed (Yoon & Langer 2005). Because these objects do enter a nebular phase and have possible SD progenitors, we include these SNe Ia in our preferred sample.

For completeness and comparison to the literature, we also derive mass limits using the prior models of Marietta et al. (2000) and

Table 3. Statistics for each sample considered in our study (see Section 4). N is the number of SNe Ia with $M_{\rm st} < M_{\rm cut}$ and $f_{n\sigma}$ is the $n\sigma$ fractional upper limit on their occurrence. $N_{\rm tot}$ refers to the total number of SNe Ia in that sample.

		H rich ($M_{\rm st,H} < 0.15\,{\rm M}_\odot$)			He rich ($M_{\rm st,He} < 0.023\,{\rm M}_\odot$)		
Sample	$N_{\rm tot}$	N	$f_{1\sigma}$	$f_{3\sigma}$	N	$f_{1\sigma}$	$f_{3\sigma}$
Normal	90	86	< 1.3 per cent	< 6.6 per cent	73	< 1.5 per cent	< 7.7 per cent
91T-like	5	5	< 17.4 per cent	< 62.7 per cent	4	< 20.5 per cent	< 69.4 per cent
91bg-like	8	8	< 12.0 per cent	< 48.2 per cent	7	< 13.4 per cent	< 52.3 per cent
SC	4	4	< 20.5 per cent	< 69.4 per cent	4	< 20.5 per cent	< 69.4 per cent
Iax	4	4	< 20.5 per cent	< 69.4 per cent	4	< 20.5 per cent	< 69.4 per cent
Normal + 91T	95	91	< 1.2 per cent	< 6.2 per cent	77	< 1.5 per cent	< 7.3 per cent
Normal + 91bg	98	94	< 1.2 per cent	< 6.0 per cent	80	< 1.4 per cent	< 7.0 per cent
Normal+91T + 91bg	103	99	< 1.1 per cent	< 5.7 per cent	84	< 1.3 per cent	< 6.7 per cent
Normal+91T+91bg + SC	107	103	< 1.1 per cent	< 5.5 per cent	88	< 1.3 per cent	< 6.4 per cent
All	111	107	< 1.1 per cent	< 5.3 per cent	92	< 1.2 per cent	< 6.2 per cent

Mattila et al. (2005), which are shown in Fig. 8. Considering the same preferred *Normal+91T+91bg + SC* sample, we still rule out H-rich non-degenerate companions ($M_{\rm st,H} < 0.15\,{\rm M}_\odot$) for 60 SNe Ia, corresponding to a 1σ (3σ) fractional upper limit of < 1.9 per cent (< 9.2 per cent). This result differs slightly from the upper limit provided in Table 3 due to the assumed linear scaling between stripped mass and emitted luminosity (e.g. Leonard 2007).

In addition to the observational limitations discussed in Section 3, the models used in this work are developed for normal SNe Ia. Overluminous and underluminous explosions will likely differ in the amount of stripped material from a companion star due to the differing expansion velocities (e.g. Benetti et al. 2005; Blondin et al. 2012; Folatelli et al. 2013) and amount of ejecta mass (e.g. Cappellaro et al. 1997; Scalzo et al. 2014, 2019). Additionally, the SN luminosity depends on the amount of Ni synthesized in the explosion (e.g. Arnett 1982; Cappellaro et al. 1997; Stritzinger et al. 2006b), indicating SNe Ia with lower Ni mass will have less gamma-ray production to power the Hα emission (i.e. a reduced $L_{\rm H\alpha}$). These effects likely superimpose, as underluminous SNe Ia will strip less mass and synthesize less Ni, but the magnitude of these effects is currently unexplored in the literature. We encourage the modelling of other SN Ia subtypes in future works.

5.2 The exclusion of SNe Ia-CSM

SNe Ia-CSM, which show interaction with a nearby circumstellar environment, are a rare class of thermonuclear explosions for which SN 2002ic is the prototype (Wang et al. 2004). These events preferentially occur in star-forming host galaxies and generally have broad, overluminous light curves ($M_{\rm R} \sim -20$ mag, Silverman et al. 2013). The observed Hα emission in SNe Ia-CSM usually appears near maximum light, has luminosities of $L_{\rm H\alpha} \sim 10^{40-41}$ ergs s^{-1}, and have velocity widths of the order of ∼2000 km s^{-1}. SNe Ia-CSM are broadly thought to stem from SD progenitor systems (e.g. Han & Podsiadlowski 2006), although DD progenitors have also been proposed (Livio & Riess 2003).

Even among this rare class of SNe Ia, there are peculiar events that do not conform to the 'standard' properties. In particular, ASASSN-18tb (Kollmeier et al. 2019; Vallely et al. 2019b) was an underluminous explosion, occurred in an elliptical host galaxy with little star formation, and had (comparatively) weak Hα emission ($L_{\rm H\alpha} \sim 10^{38}$ ergs s^{-1}), inconsistent with typical SNe Ia-CSM. Additionally, there are cases where the Hα emission does not appear until later in the SN's evolution, referred to as 'delayed-onset' SNe Ia-CSM (e.g. Graham et al. 2019).

Hα emission is also expected for material stripped from a companion, therefore differentiating between SNe Ia-CSM and SNe Ia with stripped material emission is an important distinction. Stripped companion material will have significantly lower velocities than the expanding SN ejecta ($v_{\rm strip} \sim 10^3$ km s^{-1} versus $v_{\rm ej} \sim 10^4$ km s^{-1}), shrouding the H-emitting material with the optically thick photosphere until the SN enters the nebular phase (∼150–180 d after maximum light). Thus, we exclude all objects with broad Hα detected < 100 d after maximum light. The only SN Ia-CSM that passes this criterion is SN 2015cp, a delayed-onset SN Ia-CSM (Graham et al. 2019).

While it is possible that the Hα emission observed in SN 2015cp is from material stripped from a companion, we find this scenario unlikely. The classification spectrum taken by PESSTO (Smartt et al. 2015b) at ∼45 d after maximum excludes the presence of PTF11kx-like Hα emission at 10σ (Graham et al. 2019). The next spectrum was acquired at ∼700 d after maximum light and exhibited broad Hα emission with $v_{\rm FWHM} \approx 2400$ km s^{-1} and $L_{\rm H\alpha} \approx 10^{38}$ ergs s^{-1}. This measured $L_{\rm H\alpha}$ is an order of magnitude higher than the Hα luminosity extrapolated from equation (1) at ∼710 d after explosion, although the models have not been tested at these epochs. Additionally, the Hα flux decreases sharply at ∼730 d after peak by a factor of ≈3 over the span of ∼90 d, inconsistent with Hα emission powered by radioactively decaying SN ejecta that would roughly follow the SN bolometric luminosity. These properties are consistent with CSM interaction, attributing the abrupt flux decrement to the shock passing through the CSM material. For these reasons, we consider SN 2015cp a likely SN Ia-CSM and exclude it from our analysis, although further modelling is encouraged to definitively determine mass estimates.

5.3 Time-variable and blue-shifted sodium absorption

Another subset of SNe Ia with interesting properties is objects with time-varying and blue-shifted NaID absorption, for which SN 2006X is the prototype (Patat et al. 2007). The NaID absorption is thought to stem from NaID material near the explosion that photoionizes during the early phases of the explosion and produces the absorption lines as the NaID material cools and recombines (e.g. Simon et al. 2009). However, the origin of the NaID material is unclear and proposed sources include wind from an SD progenitor system (e.g. Patat et al. 2007), circumstellar debris from a DD merger (e.g. Raskin & Kasen 2013), or even nearby gas clouds within the host galaxy (Chugai 2008).

Sternberg et al. (2011) analysed a set of 35 SNe Ia and found that 22 exhibit some form of NaID absorption profiles, with 12 having blue-shifted (relative to the host-galaxy velocity) NaID profiles. However, comparing their SN Ia sample to a sample of core-collapse (CC) SNe they could not statistically confirm that the two sets come from different parent populations (i.e. the source for SNe Ia and CC SNe NaID absorption could be the same). Additionally, the blue-shifted NaID profiles are preferentially observed in spiral galaxies, indicating that age or host-galaxy environment may play a role in the NaID interpretation.

Another prediction for NaID absorption associated with the SN Ia progenitor system is a time-variable NaID equivalent width, as the NaID material will recombine at different times depending on the distance from the explosion. Sternberg et al. (2014) searched for time-varying NaID absorption in a sample of 14 objects and found 3 SNe Ia that meet this criterion (PTF11kx, SNe 2006X, and 2007le). With these detections, Sternberg et al. (2014) found that 18 ± 11 per cent of SNe Ia have variable NaID profiles and thus could be produced by an SD progenitor system, in conflict with the results presented here. One of these objects is a known SN Ia-CSM that we exclude from the sample (PTF11kx, Dilday et al. 2012), but SNe 2006X and 2007le are both in our nebular sample and have strict constraints on stripped companion material ($M_{\rm st} < 4 \times 10^{-5}\,{\rm M}_{\odot}$ for SN 2006X and $M_{\rm st} < 3 \times 10^{-3}\,{\rm M}_{\odot}$ for SN 2007le). We discuss these discrepancies further in Section 5.4.

5.4 The lack of a consistent theory for SN Ia progenitors

Besides this work, there are several other studies that place quantitative or qualitative limits on the fraction of SD progenitor systems using a range of wavelengths and techniques (e.g. Gilfanov & Bogdán 2010; Hayden et al. 2010; Bianco et al. 2011; Brown et al. 2012; Chomiuk et al. 2016). Most of these studies focus on WD + RG systems, as these are the easiest to observationally detect. Each study individually does not definitively rule out SD SN Ia progenitors; however, when considered as a whole it is clear that most SNe Ia cannot form through the classical SD scenario. Thus, the DD scenario likely accounts for the majority of normal SNe Ia. However, detecting and characterizing double WD binaries are exceptionally difficult (e.g. Rebassa-Mansergas et al. 2018).

Reconciling limits on SD progenitors with SD-favoured SNe (i.e. SNe Ia-CSM and SNe Ia with variable NaID) has long been a difficulty for the community. The systems with conflicting interpretations, such as SN 2007le and ASASSN-18bt, are especially interesting. SN 2007le exhibits time-variable, blue-shifted NaID absorption (Sternberg et al. 2014) but has stringent limits on stripped material emission (this work, Table B5). Similarly, ASASSN-18bt showed a two-component rising light curve (Dimitriadis et al. 2019b; Shappee et al. 2019), a potential signature for SN ejecta impacting a nearby companion (Kasen 2010). However, nebular spectra rule out any stripped material emission with strict upper limits (Tucker et al. 2018; Dimitriadis et al. 2019a, this work). While the discrepancies for both SNe Ia can also be explained with alternative theories (e.g. Ni^{56} mixing for the two-component rise in ASASSN-18bt and DD merger debris for the NaID absorption in SN 2007le), these objects highlight the uncertainties that still surround SN Ia progenitors.

Recently, ATLAS18qtd (SN 2018cqj) was discovered to exhibit time-variable Hα emission in the nebular phase (Prieto et al. 2019). The spectra were posted after the submission of this manuscript; however, it warrants a brief discussion here. The classification spectrum taken at 19 d after maximum has no evidence for H emission, and the next spectrum was not acquired until ∼190 d after maximum. The measured Hα luminosity declines contemporaneously with the SN Ia luminosity, a key expectation for material stripped from an SD progenitor. However, there are only two measurements of the Hα emission and the inferred mass of the stripped material ($M_{\rm st} \approx 10^{-3}\,{\rm M}_{\odot}$) is far lower than expected (∼0.1–0.5 $\rm M_{\odot}$). ATLAS18qtd is an underluminous explosion, so it is possible the stripped material will be lower than expected from simulations in the literature, but the extent of these effects is still unexplored. Late-time observations of this unique object may yet further constrain the evolution of the Hα emission and help elucidate its origin. If we assume that ATLAS18qtd is indeed an SD progenitor system, this discovery highlights the inherent rarity of such events compared to the typical SN Ia population.

There is also the possibility that stripped material does exist in our sample but is invisible due to observational factors. The radioactively decaying SN Ia ejecta provide a power source for the stripped material, namely gamma-ray deposition. Since we only analyse spectra that are in the nebular phase, we are probing the innermost regions of the explosion. SNe Ia at these epochs essentially have no photosphere, and thus have no way of shrouding the Hα-emitting material. No such mechanism or process has been proposed to suppress the expected Hα emission, so we consider this possibility unlikely. We conclude that most SNe Ia cannot have formed from a classical SD progenitor system based on this work.

6 CONCLUSION

We present a large, comprehensive search for emission expected from stripped companion material in the SD formation scenario of SNe Ia. Using 227 spectra of 111 SNe Ia from a variety of telescopes and instruments, we find no evidence for any stripped material emission in our sample. Using these null detections, we place statistical constraints on the fraction of SNe Ia that can form through the classical RLOF SD scenario, finding that < 5.5 and < 6.4 per cent of SNe Ia can form through the H-rich and He-rich channels, respectively, at 3σ confidence. The lack of emission is difficult to reconcile with the classical SD formation scenario for SNe Ia, and provides unique constraints on the production mechanism of these phenomena.

Thus far, there has not been a proposed formation mechanism that adequately reproduces all aspects of SN Ia properties. There seems to be contributions from both SD and DD progenitors to the total SN Ia rate (e.g. section 4.1 from Maoz et al. 2014), yet the exact distribution is widely debated. Reconciling seemingly conflicting results (e.g. this work versus Sternberg et al. 2014) has long been a difficulty. Any unifying theory for SN Ia formation must account for all the observed characteristics of these phenomena and the seemingly conflicting results across various methodologies. If the SD channel does produce a significant fraction of SNe Ia, there must be an unincorporated physical process in previous modelling efforts to explain our non-detections of stripped material. Alternatively, most SNe Ia must form from DD systems to match the results presented here.

Facilities: duPont, Magellan, Very Large Telescope.

Software: Python2.7, astropy (The Astropy Collaboration 2018), astroquery (Ginsburg et al. 2019) numpy, scipy, PyMUSE (Pessa et al. 2018), SpectRes (Carnall 2017), extinction,[15] SExtractor

[15] https://github.com/kbarbary/extinction

(Bertin & Arnouts 1996), Montage,[16] Lpipe, IDL8.6, LowRedux, IRAF, and SNooPy (Burns et al. 2011).

ACKNOWLEDGEMENTS

We thank K. Maguire, K. Graham, K. Motohara, K. Maeda, S. Taubenberger, T. Diamond, G. Dimitriadis, C. Ashall, and D. Sand for supplying nebular spectra. We thank A. Laity for assisting with the KOA data search and retrieval. Additionally, we thank C. Auge, G. Anand, A. Payne, and O. Graur for useful conversations about the project. We thank P. Chen for providing several SN Ia light curves prior to publication. Also, many thanks to Bev Wills for her help tracking down the information regarding the nebular spectrum of SN 1981B.

MAT acknowledges support from the United States Department of Energy through the Computational Sciences Graduate Fellowship (DOE CSGF) through grant DE-SC0019323. BJS is supported by NSF grants AST-1908952, AST-1920392, and AST-1911074. MDS is supported in part by a generous grant (13261) from Villum Fonden and a project grant from the Independent Research Fund Denmark. Support for JLP is provided in part by FONDECYT through the grant 1191038 and by the Ministry of Economy, Development, and Tourism's Millennium Science Initiative through grant IC120009, awarded to The Millennium Institute of Astrophysics, MAS. PJV is supported by the National Science Foundation Graduate Research Fellowship Program under grant no. DGE-1343012. CSK is supported by NSF grants AST-1515876, AST-1515927, and AST-181440. CSK is also supported by a fellowship from the Radcliffe Institute for Advanced Study at Harvard University.

This work is based on (in part) observations collected at the European Organisation for Astronomical Research in the Southern hemisphere under ESO programmes 0100.D-0191(A), 0101.D-0173(A), 0102.D-0287(A), and 096.D-0296(A). This paper includes data gathered with the 6.5 m Magellan Telescopes located at Las Campanas Observatory, Chile. The CSP has been supported by the National Science Foundation under grants AST0306969, AST0607438, AST1008343, AST1613426, and AST1613472.

This paper made use of the modsIDL spectral data reduction reduction pipeline developed in part with funds provided by NSF grant AST-1108693.

This research made use of Montage. It is funded by the National Science Foundation under grant number ACI-1440620, and was previously funded by the National Aeronautics and Space Administration's Earth Science Technology Office, Computation Technologies Project, under Cooperative Agreement Number NCC5-626 between NASA and the California Institute of Technology.

This work has made use of data from the European Space Agency (ESA) mission *Gaia* (https://www.cosmos.esa.int/gaia), processed by the *Gaia* Data Processing and Analysis Consortium (DPAC; https://www.cosmos.esa.int/web/gaia/dpac/consortium). Funding for the DPAC has been provided by national institutions, in particular the institutions participating in the *Gaia* Multilateral Agreement.

The Pan-STARRS1 Surveys (PS1) and the PS1 public science archive have been made possible through contributions by the Institute for Astronomy, the University of Hawaii, the Pan-STARRS Project Office, the Max-Planck Society and its participating institutes, the Max Planck Institute for Astronomy, Heidelberg and the Max Planck Institute for Extraterrestrial Physics, Garching, The Johns Hopkins University, Durham University, the University of Edinburgh, the Queen's University Belfast, the Harvard-Smithsonian Center for Astrophysics, the Las Cumbres Observatory Global Telescope Network Incorporated, the National Central University of Taiwan, the Space Telescope Science Institute, the National Aeronautics and Space Administration under grant no. NNX08AR22G issued through the Planetary Science Division of the NASA Science Mission Directorate, the National Science Foundation grant no. AST-1238877, the University of Maryland, Eotvos Lorand University (ELTE), the Los Alamos National Laboratory, and the Gordon and Betty Moore Foundation.

Based on observations obtained at the Gemini Observatory acquired through the Gemini Observatory Archive and processed with the Gemini PyRAF package, which is operated by the Association of Universities for Research in Astronomy, Inc., under a cooperative agreement with the NSF on behalf of the Gemini partnership: the National Science Foundation (United States), the National Research Council (Canada), CONICYT (Chile), Ministerio de Ciencia, Tecnología e Innovación Productiva (Argentina), and Ministério da Ciência, Tecnologia e Inovação (Brazil).

This paper makes use of data obtained from the Isaac Newton Group of Telescopes Archive, which is maintained as part of the CASU Astronomical Data Centre at the Institute of Astronomy, Cambridge.

The LBT is an international collaboration among institutions in the United States, Italy, and Germany. LBT Corporation partners are: The University of Arizona on behalf of the Arizona Board of Regents; Istituto Nazionale di Astrofisica, Italy; LBT Beteiligungsgesellschaft, Germany, representing the Max-Planck Society, The Leibniz Institute for Astrophysics Potsdam, and Heidelberg University; The Ohio State University, and The Research Corporation, on behalf of The University of Notre Dame, University of Minnesota, and University of Virginia.

[16]http://montage.ipac.caltech.edu/

REFERENCES

Amanullah R. et al., 2014, ApJ, 788, L21
Andersen J. et al., 1995, The Messenger, 79, 12
Angel J. R. P. et al., 1979, in Weekes T. C., ed., The MMT and the Future of Ground-Based Astronomy, SAO Special Report #385. p. 87
Antognini J. M. et al., 2014, MNRAS, 439, 1079
Appenzeller I. et al., 1998, The Messenger, 94, 1
Arcavi I. et al., 2014, Astron. Telegram, 6661, 1
Ardeberg A. et al., 1973, A&A, 28, 295
Arnett W. D., 1982, ApJ, 253, 785
Bacon R. et al., 2010, in Ian S. M., Suzanne K. R., Hideki T., eds, Proc. SPIE Conf. Ser. Vol. 7735, Ground-based and Airborne Instrumentation for Astronomy III. SPIE, Bellingham, p. 773508
Barbon R. et al., 1972, Int. Astron. Union Circ., 2411, 1
Benetti S. et al., 2004, MNRAS, 348, 261
Benetti S. et al., 2005, ApJ, 623, 1011
Benn C. et al., 2008, in McLean I. S., Casali M. M., eds, Proc. SPIE Conf. Ser. Vol. 7014, Ground-based and Airborne Instrumentation for Astronomy II. SPIE, Bellingham, p. 70146X
Bertin E. et al., 1996, A&AS, 117, 393
Bianco F. B. et al., 2011, ApJ, 741, 20
Black C. S. et al., 2016, MNRAS, 462, 649
Blakeslee J. P. et al., 2010, ApJ, 724, 657
Blondin S. et al., 2012, AJ, 143
Boehner P. et al., 2017, MNRAS, 465, 2060
Botyánszki J. et al., 2017, ApJ, 845
Botyánszki J. et al., 2018, ApJ, 852
Branch D. et al., 1993, AJ, 106, 2383
Breare J. M. et al., 1987, MNRAS, 227, 909

Brown P. J. et al., 2012, ApJ, 749
Brown P. J. et al., 2015, ApJ, 805, 74
Buckley D. A. H. et al., 2006, in Ian S. M., Masanori I., eds, Proc. SPIE Conf. Ser. Vol. 6269, Ground-based and Airborne Instrumentation for Astronomy. SPIE, Bellingham, p. 62690A
Burns C. R. et al., 2011, AJ, 141
Burns C. R. et al., 2014, ApJ, 789, 32
Buzzoni B. et al., 1984, The Messenger, 38, 9
Canal R. et al., 2001, ApJ, 550, L53
Cappellaro E. et al., 1997, A&A, 328, 203
Cappellaro E. et al., 2001, ApJ, 549, L215
Carnall A. C., 2017, preprint (arXiv:1705.05165)
Cepa J., 2010, Astrophys. Space Sci. Proc., 14, 15
Chambers K. C. et al., 2016, preprint (arXiv:1612.05560)
Chen P. et al., 2019, ApJ, 880, 35
Childress M. J. et al., 2016, PASA, 33, e055
Chomiuk L. et al., 2016, ApJ, 821, 119
Chugai N. N., 1986, Sov. Astron., 30, 563
Chugai N. N., 2008, Astron. Lett., 34, 389
Contreras C. et al., 2010, AJ, 139, 519
Cousins A. W. J., 1972, Inf. Bull. Var. Stars, 700, 1
Cristiani S. et al., 1992, A&A, 259, 63
D'Odorico S., 1990, The Messenger, 61, 51
Di Stefano R. et al., 2011, ApJ, 738, L1
Dilday B. et al., 2012, Science, 337, 942
Dimitriadis G. et al., 2014, Astron. Telegram, 6749, 1
Dimitriadis G. et al., 2019a, ApJ, 870, L14
Dimitriadis G. et al., 2019b, ApJ, 870, L1
Dong S. et al., 2015a, MNRAS, 454, L61
Dong S. et al., 2018a, MNRAS, 479, L70
Dopita M. et al., 2007, Ap&SS, 310, 255
Dopita M. et al., 2010, Ap&SS, 327, 245
Dressler A. et al., 2011, PASP, 123, 288
Evans D. W. et al., 2018, A&A, 616, A4
Faber S. M. et al., 2003, in Iye M., Moorwood A. F. M., eds, Proc. SPIE Conf. Ser. Vol. 4841, Instrument Design and Performance for Optical/Infrared Ground-based Telescopes. SPIE, Bellingham, p. 1657
Fabricant D. et al., 1998, PASP, 110, 79
Fink M. et al., 2010, A&A, 514, A53
Firth R. E. et al., 2015, MNRAS, 446, 3895
Fitzpatrick E. L., 1999, PASP, 111, 63
Flewelling H. A. et al., 2016, preprint (arXiv:1612.05243)
Folatelli G. et al., 2010a, AJ, 139, 120
Folatelli G. et al., 2013, ApJ, 773
Foley R. J. et al., 2013, ApJ, 767, 57
Foley R. J. et al., 2014, MNRAS, 443, 2887
Foley R. J. et al., 2015, ApJ, 798, L37
Foley R. J. et al., 2016, MNRAS, 461, 433
Freedman W. L. et al., 2001, ApJ, 553, 47
Freudling W. et al., 2013, A&A, 559, A96
Frye R. et al., 1972, Int. Astron. Union Circ., 2398, 1
Fukugita M. et al., 1996, AJ, 111, 1748
Gaia Collaboration, 2016, A&A, 595, A1
Gaia Collaboration, 2018, A&A, 616, A1
Galbany L. et al., 2016, MNRAS, 457, 525
Ganeshalingam M. et al., 2010, ApJS, 190, 418
Gao J. et al., 2015, ApJ, 807, L26
Gilfanov M. et al., 2010, Nature, 463, 924
Ginsburg A. et al., 2019, preprint (arXiv:1901.04520)
Gomez G. et al., 1996, AJ, 112, 2094
Graham M. L. et al., 2017, MNRAS, 472, 3437
Graham M. L. et al., 2019, ApJ, 871, 62
Guillochon J. et al., 2017, ApJ, 835
Hamuy M. et al., 2006, PASP, 118, 2
Han Z. et al., 2006, MNRAS, 368, 1095
Hayden B. T. et al., 2010, ApJ, 722, 1691
Holmbo S. et al., 2018, A&A, 627, A174
Holoien T. W. S. et al., 2014, Astron. Telegram, 6637, 1
Holoien T. W. S. et al., 2017a, MNRAS, 464, 2672
Holoien T. W. S. et al., 2017b, MNRAS, 467, 1098
Holoien T. W. S. et al., 2017c, MNRAS, 471, 4966
Holoien T. W. S. et al., 2019, MNRAS, 93
Hook I. M. et al., 2004, PASP, 116, 425
Howell D. A., 2001, ApJ, 554, L193
Howell D. A. et al., 2006, Nature, 443, 308
Hoyle F. et al., 1960, ApJ, 132, 565
Huang X. et al., 2017, ApJ, 836, 157
Iben I. et al., 1984, ApJS, 54, 335
Jha S. et al., 2006, AJ, 131, 527
Jha S. W. et al., 2019, Nature Astronomy, 3, 706
Jones D. H. et al., 2009, MNRAS, 399, 683
Jorden P. R., 1990, in David L. C., ed., Proc. SPIE Conf. Ser. Vol. 1235, Instrumentation in Astronomy VII. SPIE, Bellingham, p. 790
Justham S., 2011, ApJ, 730, L34
Kasen D., 2010, ApJ, 708, 1025
Kashikawa N. et al., 2002, PASJ, 54, 819
Katz B. et al., 2012, preprint (arXiv:1211.4584)
Kelson D. D., 2003, PASP, 115, 688
Kelson D. D. et al., 2000, ApJ, 531, 159
Kirshner R. P. et al., 1975, ApJ, 200, 574
Kiyota S. et al., 2014a, Astron. Telegram, 6594, 1
Kiyota S. et al., 2014b, Astron. Telegram, 6683, 1
Kollmeier J. A. et al., 2019, MNRAS, 486, 3041
Krisciunas K. et al., 2017, AJ, 154, 211
Kromer M. et al., 2010, ApJ, 719, 1067
Lanz T. et al., 2005, ApJ, 619, 517
Larsen S. S. et al., 2001, AJ, 121, 2974
Lee T. A. et al., 1972, ApJ, 177, L59
Leonard D. C., 2007, ApJ, 670, 1275
Leonard D. C. et al., 2001, PASP, 113, 920
Li W. et al., 2003a, PASP, 115, 453
Li W. et al., 2019, ApJ, 870, 12
Liu Z.-W. et al., 2013a, ApJ, 774, 37
Liu Z.-W. et al., 2013b, ApJ, 778, 121
Liu Z. W. et al., 2012, A&A, 548, A2
Livio M. et al., 2003, ApJ, 594, L93
Livio M. et al., 2018, Phys. Rep., 736, 1
Livne E., 1990, ApJ, 354, L53
Livne E. et al., 1995, ApJ, 452, 62
Li W. D. et al., 2000, in Holt S. S. et al., eds, AIP Conf. Proc. Vol. 522, Cosmic Explosions. Am. Inst. Phys., New York, p. 103
Lundqvist P. et al., 2013, MNRAS, 435, 329
Lundqvist P. et al., 2015, A&A, 577, A39
Maguire K. et al., 2016, MNRAS, 457, 3254
Maoz D. et al., 2014, ARA&A, 52, 107
Marietta E. et al., 2000, ApJS, 128, 615
Marshall J. L. et al., 2008, in McLean I. S., Casali M. M., eds, Proc. SPIE Conf. Ser. Vol. 7014, Ground-based and Airborne Instrumentation for Astronomy II. SPIE, Bellingham, p. 701454
Matheson T. et al., 2008, AJ, 135, 1598
Mattila S. et al., 2005, A&A, 443, 649
Mazzali P. A. et al., 2015, MNRAS, 450, 2631
McCully C. et al., 2014, Nature, 512, 54
Meng X. et al., 2013, ApJ, 778, L35
Molinari E. et al., 1999, in Faffaella M., Warrick J. C., eds, Proc. ESO, Looking Deep in the Southern Sky. Springer-Verlag, Berlin, p. 157
Moorwood A. et al., 1998, The Messenger, 91, 9
Morrell N. et al., 2014a, Astron. Telegram, 6508, 1
Motohara K. et al., 2002, PASJ, 54, 315
Nicolas J. et al., 2014, Astron. Telegram, 6500, 1
Nomoto K., 1982, ApJ, 253, 798
Oke J. B. et al., 1982, PASP, 94, 586
Oke J. B. et al., 1995, PASP, 107, 375
Osmer P. S. et al., 1972, Nat. Phys. Sci., 238, 21
Pakmor R. et al., 2012, ApJ, 747, L10
Pan K.-C. et al., 2012, ApJ, 750, 151

Patat F. et al., 2007, Science, 317, 924
Pejcha O. et al., 2013, MNRAS, 435, 943
Pessa I. et al., 2018, preprint (arXiv:1803.05005)
Phillips M. M. et al., 2007, PASP, 119, 360
Phillips M. M. et al., 2013, ApJ, 779, 38
Phillips M. M. et al., 2019, PASP, 131, 014001
Pogge R. W. et al., 2010, in Ian S. M., Suzanne K. R., Hideki T., eds, Proc. SPIE Conf. Ser. Vol. 7735, Ground-based and Airborne Instrumentation for Astronomy III. SPIE, Bellingham, p. 77350A
Press W. H. et al., 1992, Numerical Recipes in FORTRAN. The Art of Scientific Computing
Prieto J. L. et al., 2019, preprint (arXiv:1909.05267)
Przybylski A., 1972, Int. Astron. Union Circ., 2434, 1
Raskin C. et al., 2013, ApJ, 772, 1
Rebassa-Mansergas A., Toonen S., Korol V., Torres S., 2018, MNRAS, 482, 3656
Riello M. et al., 2018, A&A, 616, A3
Riess A. G. et al., 1999, AJ, 117, 707
Riess A. G. et al., 2016, ApJ, 826
Romero-Canizales C. et al., 2014, Astron. Telegram, 6618, 1
Röpke F. K. et al., 2012, ApJ, 750, L19
Ruffini N. J. et al., 2019, MNRAS, 489, 420
Saha A. et al., 2006, ApJS, 165, 108
Sand D. J. et al., 2018a, ApJ, 863, 24
Sand D. J. et al., 2019, ApJ, 877, L4
Saulder C. et al., 2016, A&A, 596, A14
Scalzo R. A. et al., 2014, MNRAS, 445, 2535
Scalzo R. A. et al., 2019, MNRAS, 483, 628
Schlegel D. J. et al., 1998, ApJ, 500, 525
Shappee B. J. et al., 2013, ApJ, 766
Shappee B. J. et al., 2013a, ApJ, 762
Shappee B. J. et al., 2013b, ApJ, 765, 150
Shappee B. J. et al., 2014a, ApJ, 788, 48
Shappee B. J. et al., 2017, ApJ, 841, 48
Shappee B. J. et al., 2018, ApJ, 855, 6
Shappee B. J. et al., 2019, ApJ, 870, 13
Sheinis A. I. et al., 2002, PASP, 114, 851
Shen K. J. et al., 2018, preprint (arXiv:1804.11163)
Silverman J. M. et al., 2012, MNRAS, 425, 1789
Silverman J. M. et al., 2013, MNRAS, 430, 1030
Simon J. D. et al., 2009, ApJ, 702, 1157
Smartt S. J. et al., 2015b, A&A, 579, A40
Springob C. M. et al., 2014, MNRAS, 445, 2677
Sternberg A. et al., 2011, Science, 333, 856
Sternberg A. et al., 2014, MNRAS, 443, 1849
Stritzinger M. et al., 2006a, A&A, 460, 793
Stritzinger M. et al., 2006b, A&A, 460, 793
Stritzinger M. D. et al., 2011, AJ, 142
Stritzinger M. D. et al., 2015, A&A, 573, A2
Taam R. E., 1980, ApJ, 237, 142
Taubenberger S. et al., 2013a, MNRAS, 432, 3117
The Astropy Collaboration, 2018, AJ, 156, 123
Theureau G. et al., 2007, A&A, 465, 71
Thompson T. A., 2011, ApJ, 741, 82
Tonry J. L. et al., 2001, ApJ, 546, 681
Tonry J. L. et al., 2012, ApJ, 750, 99
Tucker M. A. et al., 2018, ApJ, 872, L22
Tully R. B. et al., 2013, AJ, 146, 86
Tutukov A. et al., 1996, MNRAS, 280, 1035
Tutukov A. V., Yungelson L. R., 1979, Acta Astron., 29, 665
Tutukov A. V. et al., 1994, MNRAS, 268, 871
Tutukov A. V. et al., 2007, Astron. Rep., 51, 291
Vallely P. J. et al., 2019a, preprint (arXiv:1902.00037)
Vallely P. J. et al., 2019b, MNRAS, 487, 2372
van Genderen A. M., 1975, A&A, 45, 429
Vernet J. et al., 2011, A&A, 536
Villegas D. et al., 2010, ApJ, 717, 603
Wang L. et al., 2004, ApJ, 604, L53
Wang X. et al., 2008, ApJ, 675, 626
Webbink R. F., 1984, ApJ, 277, 355
Wheeler J. C. et al., 1975, ApJ, 200, 145
Whelan J. et al., 1973, ApJ, 186, 1007
Wills B. J. et al., 1980, ApJ, 237, 319
Woods T. E. et al., 2018, ApJ, 863, 120
Woosley S. E. et al., 1994, ApJ, 423, 371
Yaron O. et al., 2012, PASP, 124, 668
Yoon S. C. et al., 2003, A&A, 412, L53
Yoon S. C. et al., 2005, A&A, 435, 967

SUPPORTING INFORMATION

Supplementary data are available at *MNRAS* online.

Table B2. All SNe Ia studied in this work.
Table B3. SN Ia light-curve parameters, the number of late-time spectra, and the corresponding phases, ordered by t_{max}.
Table B4. Spectra observations.
Table B5. Flux limits for each line in Table 2 and the corresponding H/He mass limit.
Table B6. New photometry presented in this study.
Table B7. Photometry data for each SN Ia studied in this work.

Please note: Oxford University Press is not responsible for the content or functionality of any supporting materials supplied by the authors. Any queries (other than missing material) should be directed to the corresponding author for the article.

APPENDIX A: A NEBULAR PHASE PHILLIP'S RELATION

In most SNe Ia, the peak luminosity and photospheric phase decline rate (e.g. Δm_{15}) are correlated with the amount of ^{56}Ni produced in the explosion (e.g. Stritzinger et al. 2006a; Scalzo et al. 2019). Therefore, these same observables should also correlate with the magnitude of SNe Ia as they enter the nebular phase. For SNe Ia with nebular spectra but no usable nebular photometry, this relation provides a method for estimating the nebular magnitude using near-peak photometry.

The photometric sample used in deriving the NPPR excludes Iax, CSM, and SC SNe Ia. Although 91T- and 91bg-like do not strictly follow the relation between luminosity and decline rate of normal SNe Ia, they are powered by the radioactive decay of ^{56}Ni to stable ^{56}Fe. As mentioned before, Δm_{15} is indicative of the amount of ^{56}Ni synthesized in the explosion, and therefore our parametrization described below still accurately models 91T- and 91bg-like SNe Ia. However, SC and Iax SNe Ia have unique ionization properties, which is further exemplified by their nebular spectra that lack the prominent [Fe II/III] and [Co II/III] emission features of their normal, 91T-, and 91bg-like counterparts (e.g. Taubenberger et al. 2013a; Foley et al. 2016). It is possible that the photometric intricacies of 91T- and 91bg-like SNe Ia are washed out by our heterogeneous sample, and more precise results can be attained with distinct samples of SNe Ia spectral types.

Taking all available nebular-phase photometry of viable SNe Ia from this work and the literature, we derive an approximate functional form for calculating the apparent magnitude of an SN Ia with a measured m_{max} and Δm_{15}. Since SNe Ia have nearly linear decays in magnitude space at nebular epochs, we use the functional form

$$m_{\lambda,\mathrm{neb}}(t_\mathrm{p}) = m_{\lambda,\mathrm{max}} + \Delta m_\lambda(t_\mathrm{p}), \quad \text{(A1)}$$

where $m_{\lambda,\mathrm{neb}}(t_\mathrm{p})$ is the nebular magnitude in filter λ at phase $t_\mathrm{p} = t - t_{max}$, $m_{\lambda,\mathrm{max}}$ is the magnitude at peak in filter λ, and Δm_λ is the

change in brightness between maximum light and t_p for that filter. By formulating our relation for individual filters, we can neglect extinction from the Milky Way and the host galaxy since the maximum light and nebular magnitude of an SN Ia will be affected equally. Thus, we parametrize Δm_λ as a function of the SN Ia's Δm_{15},

$$\Delta m_\lambda = A_\lambda(\Delta m_{15}) \times (t_p - 250\ \mathrm{d}) + \mathrm{B}_\lambda(\Delta \mathrm{m}_{15}), \quad \text{(A2)}$$

where

$$A_\lambda(\Delta m_{15}) = a_\lambda(\Delta m_{15} - 1.1\ \mathrm{mag}) + \mathrm{b}_\lambda, \quad \text{(A3)}$$

and

$$B_\lambda(\Delta m_{15}) = c_\lambda(\Delta m_{15} - 1.1\ \mathrm{mag}) + \mathrm{d}_\lambda. \quad \text{(A4)}$$

Here, $m_{\lambda,\mathrm{max}}$ is the apparent magnitude at maximum light in filter λ, $m_\lambda(t)$ is the nebular magnitude, t_p is the phase of the observations, Δm_{15} is the decline rate, and $\{a, b, c, d\}$ are the derived coefficients which are provided in Table A1. t_p and Δm_{15} are offset by typical values to reduce their covariance in the fitting process.

The coefficients in Table A1 were computed using all available nebular photometry between 150 and 500 d after maximum light. The coefficients were first approximated using a sample of well-studied SNe Ia with $\geq$5 measurements in a given filter in the temporal bounds listed above, such as SNe 2011fe, 2012fr, 2013gy, and 2015F, then expanded to include all photometric points. The SNe Ia used in deriving the NPPR have decline rates that span $\Delta m_{15} \sim 0.8$–1.8 mag and are denoted with a * in Table B7. For publicly available photometry for which there are no reported uncertainties, we assign a nominal uncertainty of 0.1 mag. In fitting the data, we implement non-linear least-squares fitting coupled with a bootstrap-resampling technique to derive reasonable estimates for the uncertainties. The residuals of the best-fitting solution are shown in the left-hand panel of Fig. A1, and the collapsed distribution is provided in the right-hand panel.

For SNe Ia with a measured peak magnitude and Δm_{15}, we show that the nebular *BVR* magnitude can be approximated to $\sim$20 per cent. These results were derived using a heterogeneous data set and likely can be improved with a consistent photometric system and targeted observations across a reasonable span of Δm_{15}. This technique can also be used in identifying peculiar or strange SNe Ia that deviate from their expected brightness at a given epoch, such as 'late-onset' CSM interaction (e.g. Graham et al. 2019). Additionally, we attempted to expand this methodology to other photometric filters (e.g. *g* and *r*), but there were too few observations to build a quality model.

APPENDIX B: SUPPLEMENTARY TABLES AND FIGURES

In Table B2, we provide the name of the SN Ia, redshift, and references for discovery and classification. Table B3 provides the parameters from the light-curve fits, including time of maximum light, Δm_{15}, and the distance modulus. We also include the total number of nebular-phase spectra for that SN Ia and the corresponding phases. For information on each spectrum, including the date, telescope, instrument, and reference, see Table B4. Flux limits and derived mass limits are given in Table B5. New photometry presented in this work is provided in Table B6 and all photometry references are given in Table B7.

B1 Data tables

For SNe Ia with redshifts measured from the supernova lines near maximum light, we tweak the redshift using host galaxy emission lines when necessary. Major host galaxy lines such as Hα, Hβ, [N II], and [O III] are fitted with Gaussian line profiles to estimate the line centre and then used to measure the host redshift.

For SNe Ia with insufficient photometry for a reliable light-curve fit in `snoopy`, we consider two approaches. If there are $\geq$3 photometric points near maximum light, we use linear least-squares coupled with bootstrap-resampling to fit a quadratic curve to the data and estimate t_{max} and the associated uncertainty. Otherwise, the value for t_{max} is taken from the spectroscopic classification reference given in Table B2 and assigned a nominal uncertainty of $\pm$5 d.

SNe-Iax do not conform to the standard SN Ia templates utilized by `snoopy` and other SN Ia light-curve fitters. Thus, we compute Δm_{15} and t_{max} using spline fits in the `snoopy` environment. This prevents us from deriving the host reddening $E(B-V)_{host}$; however, the Iax SNe in our sample have negligible reddening (Li et al. 2003a; Phillips et al. 2007; McCully et al. 2014; Foley et al. 2015; Stritzinger et al. 2015).

The 'Quality' column in Table B4 provides a rough estimate of the quality of the spectrum. This is mostly qualitative, and intended to provide readers with an estimate of the spectral quality for each SN Ia in our sample. The rankings are as follows:

High: The spectrum clearly shows the major Fe and Co emission lines between $\sim$4000 and 7000 Å. The spectrum exhibits little to no host contamination or instrumental artefacts.

Med(ium): The major Fe lines are visible, while the Co lines are noisy or absent. The spectrum may also suffer from minor to moderate host galaxy contamination and/or instrumental artefacts.

Low: The major Fe lines are barely detectable above the spectral noise, and the Co lines mostly below the detection threshold. This category also includes overall medium-quality spectra with significant host galaxy contamination and/or instrumental artefacts.

B2 Special cases

We discuss any extenuating circumstances or any other relevant details about specific SNe Ia that differ from the general methodology described in Section 2. Examples include alternative flux calibration methods, spectroscopic oddities noticed in our analysis, and spectrum reference discrepancies. SNe Ia with R_V values known to deviate from the standard $R_V = 3.1$ are listed in Table B1. For ensemble studies (e.g. Phillips et al. 2013; Burns et al. 2014), we require a $\geq 3\sigma$ deviation from $R_V = 3.1$ to include the value in our calculation. When drawing R_V values from Burns et al. (2014), we implement the F99 + uniform prior results.

SN1998bu: The two nebular spectra from Cappellaro et al. (2001) do not have any specific mention in that manuscript; however, the reference on WiseRep points to this paper. Thus, we include the reference, but acknowledge we could not verify this paper was the true source for these spectra.

SN2002bo: The OSC and WiseRep also report several nebular phase NIR spectra for this SN. However, cross-referencing the reported spectra with the observational parameters given in Benetti et al. (2004), we believe the dates provided for the NIR spectra are off by a year, and these spectra are closer to a few months after

Table A1. Values of the coefficients for equations (A2)–(A4) and fit statistics. $N_{\rm tot}$ is the total number of photometric points used in each filter from $N_{\rm SN}$ SNe Ia.

Filter	a_λ [10^{-3} day^{-1}]	b_λ [10^{-2} mag day^{-1}]	c_λ	d_λ [mag]	$N_{\rm SN}$	$N_{\rm tot}$	$\bar{x}$	σ
B	$-7.66^{+0.53}_{-0.62}$	$1.443^{+0.005}_{-0.005}$	$0.48^{+0.04}_{-0.04}$	$6.168^{+0.003}_{-0.004}$	42	346	0.00	0.08
V	$-13.68^{+0.33}_{-0.37}$	$1.620^{+0.003}_{-0.003}$	$2.58^{+0.02}_{-0.02}$	$6.050^{+0.002}_{-0.002}$	67	438	0.03	0.13
R	$4.22^{+0.41}_{-0.33}$	$1.650^{+0.004}_{-0.003}$	$1.00^{+0.03}_{-0.03}$	$6.776^{+0.002}_{-0.002}$	34	286	0.00	0.09

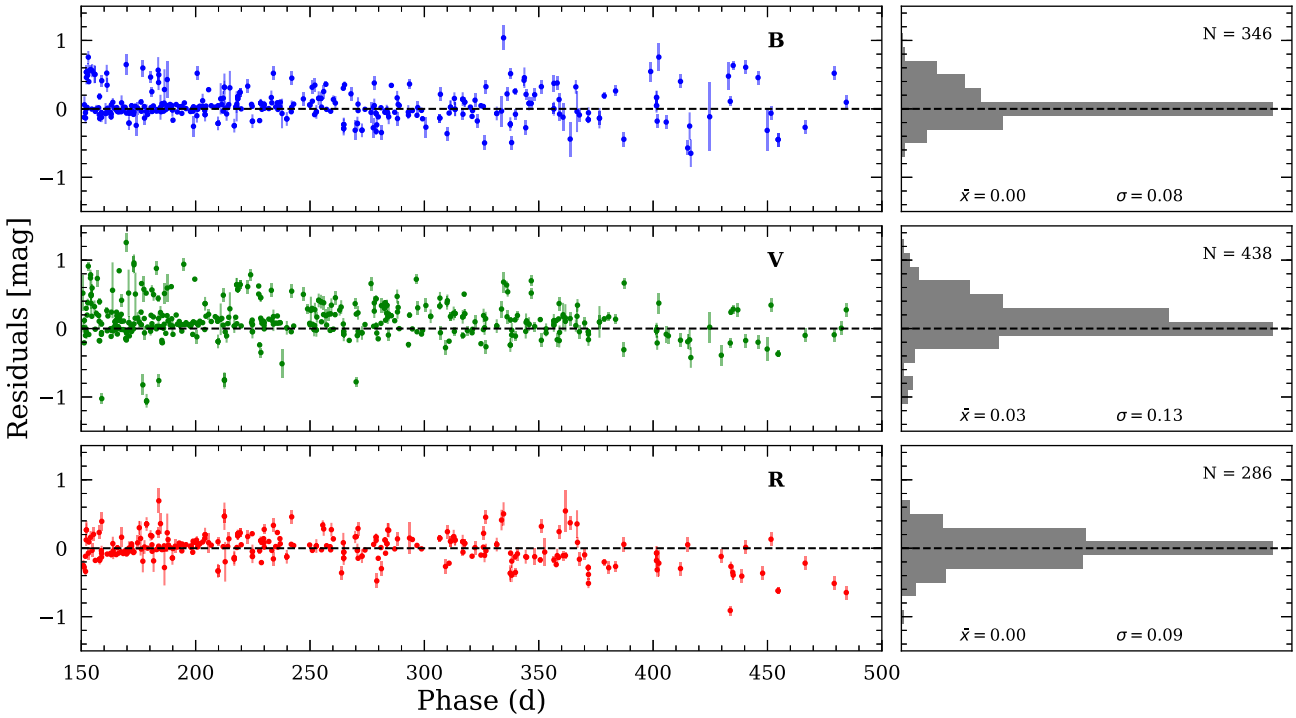

Figure A1. *Left*: Residuals of the late-time relation bootstrap fit from equations (A2)–(A4) using the values in Table A1. *Right*: Collapsed residual distribution of the best-fitting solution.

Table B1. $R_{\rm V}$ values and references for SNe Ia with $\geq 3\sigma$ deviations from the assumed $R_{\rm V} = 3.1$.

Name	$R_{\rm V}$	Ref.
SN2002bo	1.2	Phillips et al. (2013)
SN2004eo	0.8	Burns et al. (2014)
SN2006X	1.5	Wang et al. (2008); Phillips et al. (2013); Burns et al. (2014)
SN2007le	1.6	Phillips et al. (2013); Burns et al. (2014)
SN2014J	1.5	Amanullah et al. (2014); Foley et al. (2014); Gao et al. (2015); Brown et al. (2015)

maximum light instead of several hundred days after maximum light. We exclude these spectra from our sample.

B3 Supplementary figures

We provide cut-outs around each spectral line inspected for H/He emission (Table 2) for the spectrum used in calculating the limits provided in Table B5 for each SN Ia as supplementary figures. An example of the format of these figures is provided in Fig. 5. The black line is the observed spectrum, with the continuum fit and flux upper limit in red and purple, respectively. The grey shaded areas indicate masked spectral regions and completely grey boxes indicate that particular SN Ia had no spectra covering that spectral region. When multiple nebular spectra of an SN Ia cover the same expected H/He line, we provide the spectrum corresponding to the best mass limit *for that line*. Therefore, the panel for H α may show a different spectrum than the panel for Hβ for the same SN Ia. This ensures all adequate spectra are presented, even when some spectra do not cover all the optical and NIR lines considered in this study. The border colour of a given panel indicates whether it is used in the final stripped mass determination, the results of which are provided in Table B5. Blue borders indicate the panels used in the H-rich mass limit, red borders indicate He-rich limits,

Table B2. All SNe Ia studied in this work. The full table is available as supplementary material in the online manuscript.

Disc. name	IAU name	Pec?	z	Redshift ref.	Discovery	Classification
...	ASASSN-14hr	N	0.033 62	Jones et al. (2009)	Nicolas et al. (2014)	Morrell et al. (2014a)
...	ASASSN-14jc	N	0.011 32	Jones et al. (2009)	Kiyota et al. (2014a)	Romero-Canizales et al. (2014)
...	ASASSN-14jg	N	0.014 83	Jones et al. (2009)	Holoien et al. (2014)	Arcavi et al. (2014)
...	ASASSN-14jz	N	0.015 50	This Work	Kiyota et al. (2014b)	Dimitriadis et al. (2014)
...	...	...	...	...	...	...

[a]PSN J1149 = PSN J11492548-0507138.
[b]SNF-012 = SNF20080723-012.

Table B3. SNe Ia light-curve parameters, the number of late-time spectra, and the corresponding phases, ordered by t_{max}. See Section 3 for fitting methods. The full table is available as supplementary material in the online manuscript.

SN	t^a_{max} (MJD)	$\Delta m_{15}(B)$ (mag)	μ (mag)	$E(B-V)$	N_{spec}	Phase (days)
SN1972E	41445.9 ± 0.4	0.93 ± 0.06	27.75 ± 0.06[1]	−0.03 ± 0.06	4	205–418
SN1981B	44672.7 ± 0.4	1.12 ± 0.06	30.91 ± 0.05[2]	0.06 ± 0.06	1	267
SN1986G	46561.0 ± 0.4	1.57 ± 0.07	27.82 ± 0.06[1]	0.91 ± 0.06	4	256–325
SN1990N	48082.5 ± 0.3	1.09 ± 0.06	31.53 ± 0.07[2]	0.02 ± 0.06	5	186–333
...	...	...	...	...	...	...

Notes. References: (1)Tully et al. (2013); (2)Riess et al. (2016); (3)Villegas et al. (2010); (4)Freedman et al. (2001); (5)Saha et al. (2006); (6)Larsen et al. (2001); (7)Derived from redshift; (8)Theureau et al. (2007); (9)Blakeslee et al. (2010); (10)Huang et al. (2017); (11)Tonry et al. (2001); (12)Holmbo et al. (2018); (13)Saulder et al. (2016); (14)Springob et al. (2014); (15)Li et al. (2019).
[a]To be presented in P. Chen et al. (in preparation).

Table B4. Spectra observations. The full table is available as supplementary material in the online manuscript.

SN (units)	Obs. date (MJD)	Phase[a] (days)	Telescope[b]	Instrument[b]	Range (Å)	Expt. (s)	v_{exp} (km s^{-1})	Qual.	Ref.
SN1972E	41651.00	205.1	P200	DBSP	4000–10 000	...	5100 ± 800	Med	Kirshner & Oke (1975)
	41682.00	236.1	P200	DBSP	3300–10 300	...	5900 ± 400	Med	Kirshner & Oke (1975)
	41795.00	349.1	P200	DBSP	3400–10 200	...	6300 ± 100	Med	Kirshner & Oke (1975)
	41864.00	418.1	P200	DBSP	3400–9200	...	6600 ± 200	Med	Kirshner & Oke (1975)
SN1981B	44940.00	267.3	HJST	UVITS	3400–7100	3600	6200 ± 300	Med	Branch et al. (1993)
SN1986G	46816.50	255.5	ESO2.2m	BC	4500–6800	...	5500 ± 100	Med	Cristiani et al. (1992)
	46817.50	256.5	ESO3.6m	EFOSC	3700–9500	...	4900 ± 100	High	Cristiani et al. (1992)
	46818.50	257.5	ESO3.6m	EFOSC	4000–9300	...	5000 ± 200	High	Cristiani et al. (1992)
	46885.50	324.5	ESO3.6m	EFOSC	3800–7000	...	5100 ± 400	Med	Cristiani et al. (1992)
SN1990N	48268.50	186.0	WHT	FOS	3400–9700	1880	5000 ± 700	High	Gomez et al. (1996)
	48309.50	227.0	WHT	FOS	3500–9700	1800	5800 ± 600	High	Gomez et al. (1996)
	48337.50	255.0	WHT	FOS	3500–9700	1800	5800 ± 800	Med	Gomez et al. (1996)
	48362.50	280.0	WHT	FOS	3500–9700	1800	5500 ± 500	Med	Gomez et al. (1996)
	48415.50	333.0	WHT	FOS	3600–9700	2000	6100 ± 400	Med	Gomez et al. (1996)
...	...	...	...	...	...	...	...	...	...

[a]Relative to t_{max}.
[b]See Section 2 for definitions and references.

Table B5. Flux limits for each line in Table 2 and the corresponding H/He mass limit. The full table is available as supplementary material in the online manuscript.

	H-rich model				He-rich model			
SN	Phase[a] (days)	Line[b]	Flux limit (erg s^{-1} cm^{-2})	Mass limit ($M_\odot$)	Phase[a] (days)	Line[b]	Flux limit (erg s^{-1} cm^{-2})	Mass limit ($M_\odot$)
SN1972E	418.1	Hα	2.52×10^{-16}	4.95×10^{-5}	349.1	HeI-a	3.07×10^{-17}	9.84×10^{-5}
SN1981B	267.3	Hα	5.54×10^{-16}	1.49×10^{-3}	267.3	HeI-a	5.86×10^{-16}	2.25×10^{-3}
SN1986G	324.5	Hα	1.68×10^{-15}	2.84×10^{-4}	256.5	HeI-b	6.57×10^{-16}	5.29×10^{-4}
SN1990N	280.0	Hα	9.52×10^{-17}	5.68×10^{-4}	280.0	HeI-a	2.35×10^{-16}	1.53×10^{-3}
...	...	...	...	...	...	...	...	...

[a]Relative to t_{max}.
[b]Corresponds to the lines listed in Table 2.

Table B6. New photometry presented in this study. Some data stem from archival images processed by this study for flux calibration purposes. The full table is available as supplementary material in the online manuscript.

SN	MJD	Filter	AB Mag
ASASSN-14jg	57183.78	*V*	20.49 ± 0.08
ASASSN-15hx	57396.33	*V*	21.33 ± 0.04
SN2001el	52492.37	*I*	19.82 ± 0.07
SN2001el	52549.24	*I*	20.24 ± 0.07
...	...	...	...
			...

Table B7. Photometry data for each SN Ia studied in this work. $N_{\rm tot}$ refers to the total number of photometric points for a given SN. Phases are given relative to maximum light. Objects denoted with a ⋆ are used in deriving the NPPR (Appendix A). The full table is available as supplementary material in the online manuscript.

SN	$N_{\rm tot}$	Phases	Filters	Refs.
ASASSN-14jg⋆	113	$5 - 268$	*B*, *V*, *g*, *r*, *i*	ASAS-SN; Graham et al. (2017); This work
ASASSN-15hx	202	$-16 - 325$	*V*, *g*, *i*, *SwiftU*, *SwiftB*, *SwiftV*	ASAS-SN; This work
PSN J1149	16	$-12 - 141$	*B*, *V*, *I*	ASAS-SN
SN1972E⋆	468	$-23 - 359$	*U*, *B*, *V*, *R*, *I*	Przybylski (1972); Cousins (1972); Barbon et al. (1972); Ardeberg & de Groot (1973); van Genderen (1975); Osmer et al. (1972); Lee et al. (1972); Frye et al. (1972); Przybylski (1972)
...	...	...	...	...

and purple borders indicate He lines used for both H- and He-rich limits.

This paper has been typeset from a TEX/LATEX file prepared by the author.